

Whole atmosphere model simulations of ultra-fast Kelvin wave effects in the ionosphere and thermosphere

Y. Yamazaki¹, Y. Miyoshi², C. Xiong¹, C. Stolle^{1,3}, G. Soares⁴, A. Yoshikawa⁵

¹GFZ German Research Centre for Geosciences, Potsdam, Germany

²Department of Earth and Planetary Sciences, Kyushu University, Fukuoka, Japan

³Faculty of Science, University of Potsdam, Potsdam, Germany

⁴Observatório Nacional, Rio de Janeiro, Brazil

⁵International Center for Space Weather Science and Education, Kyushu University, Fukuoka, Japan

Key Points:

- GAIA model simulations of ultra-fast Kelvin wave (UFWK) in the middle and upper atmosphere
- UFWK produces eastward-propagating \sim 3-day ionospheric variations with zonal wavenumber 1
- First magnetic detection of UFWK in the equatorial electrojet

15 **Abstract**

This paper examines the response of the upper atmosphere to equatorial Kelvin waves with a period of ~ 3 days, also known as ultra-fast Kelvin waves (UFKWs). The whole atmosphere model GAIA is used to simulate the UFKW events in the late summer of 2010 and 2011 as well as in the boreal winter of 2012/2013. When the lower layers of the model below 30 km altitude are constrained with meteorological data, GAIA is able to reproduce salient features of the UFKW in the mesosphere and lower thermosphere as observed by the Aura Microwave Limb Sounder. The model also reproduces ionospheric response, as validated through comparisons with total electron content data from the GOCE satellite as well as with earlier observations. Model results suggest that the UFKW produces eastward-propagating ~ 3 -day variations with zonal wavenumber 1 in the equatorial zonal electric field and F-region plasma density. Model results also suggest that for a ground observer, identifying ionospheric signatures of the UFKW is a challenge because of ~ 3 -day variations due to other sources. This issue can be overcome by combining ground-based measurements from different longitudes. As a demonstration, we analyze ground-based magnetometer data from equatorial stations during the 2011 event. It is shown that wavelet spectra of the magnetic data at different longitudes are only in partial agreement, with or without a ~ 3 -day peak, but a spectrum analysis based on multipoint observations reveals the presence of the UFKW.

34 **1 Introduction**

Equatorial Kelvin waves are a type of global-scale waves in the atmosphere. In classical theory (Matsuno, 1966; Holton & Lindzen, 1968), they travel eastward with perturbations in the zonal velocity and geopotential but with no meridional velocity component. The amplitude is largest at the equator and it decays exponentially with latitude. Equatorial Kelvin waves propagate vertically upward from the source region in the troposphere where they are thought to be excited by latent heating due to tropical convection. They are often classified into three categories according to the wave period (and hence the zonal phase speed): slow Kelvin waves with periods 10–20 days, fast Kelvin waves with periods 5–10 days, and ultra-fast Kelvin waves (UFKWs) with periods 2–5 days. In general, a wave with a shorter period and longer wavelength is less susceptible to dissipation and thus is able to reach higher altitudes. As the wave propagates to higher altitudes, it grows in amplitude due to the reduction in atmospheric density. The

47 shortest-period waves, thus UFKWs, can propagate well into the mesosphere and lower
 48 thermosphere (MLT) region before being dissipated. Therefore, UFKWs can be a sig-
 49 nificant source of wave forcing in the upper atmosphere among other global-scale waves
 50 such as tides and planetary waves (Yigit & Medvedev, 2015; H.-L. Liu, 2016).

51 Equatorial Kelvin waves were first identified in the lower stratosphere from radiosonde
 52 measurements. Wallace and Kousky (1968) found equatorial Kelvin waves with periods
 53 ~ 15 days and vertical wavelength of ~ 10 km, which are now known as slow Kelvin waves.
 54 Hirota (1978, 1979) detected fast Kelvin waves with periods ~ 10 days and vertical wave-
 55 length 15–20 km in the upper stratosphere and lower mesosphere using rocket and satel-
 56 lite measurements. Salby et al. (1984) was the first to observe the UFKW. They found
 57 UFKWs with periods ~ 4 days and vertical wavelength ~ 40 km in the mesosphere based
 58 on the temperature data from the Nimbus-7 satellite. Lieberman and Riggan (1997) con-
 59 firmed the presence of UFKWs at altitudes between 65 and 110 km using wind measure-
 60 ments from the UARS satellite. Forbes et al. (2009), using temperature measurements
 61 from the SABER instrument on the TIMED satellite, showed a transition of dominant
 62 waves from fast Kelvin waves (periods 5–10 days and vertical wavelengths 9–13 km) in
 63 the stratosphere to UFKWs (periods 2–3 days and vertical wavelengths 35–45 km) in
 64 the MLT region. Their results also showed that for fast Kelvin waves, the zonal-wavenumber
 65 1 and zonal-wavenumber 2 components are comparable in amplitude, while for UFKWs,
 66 the zonal-wavenumber 1 component is dominant. Vincent (1993) and subsequent stud-
 67 ies (Riggan et al., 1997; Yoshida et al., 1999; Sridharan et al., 2002; Pancheva et al., 2004;
 68 Davis et al., 2012) used wind measurements from meteor radars to examine UFKWs in
 69 the MLT region. UFKW activity is usually observed in short-lived bursts, which last a
 70 few wave cycles. England et al. (2012) and Egito et al. (2018) presented evidence for non-
 71 linear interaction between UFKWs and diurnal tide, which leads to the modulation of
 72 the tidal amplitude with UFKW periodicities. W.-S. Chen et al. (2018) examined the
 73 seasonal variability of the UFKW using SABER temperature measurements during 2002–
 74 2016, pointing out that the upward-propagation of the UFKW is influenced by both the
 75 mesospheric and stratospheric semiannual oscillations. G. Liu et al. (2019), using a sim-
 76 ilar dataset, examined the interannual variability of the UFKW at 110 km. The observed
 77 year-to-year variations were attributed to changes in the solar flux as well as to the quasi-
 78 biennial oscillation and El Niño–Southern oscillation of the atmosphere. Gasperini et al.
 79 (2015, 2018) used the accelerometer data from the Gravity field and steady-state Ocean

80 Circulation Explorer (GOCE) satellite to detect UFKWs in the thermosphere at \sim 250
 81 km altitude, which was shown to be consistent with the UFKWs observed in the MLT
 82 region at the same time.

83 Studies have also shown that the UFKW can affect the ionosphere. Takahashi et
 84 al. (2006, 2007) observed \sim 3 day variations in ionospheric parameters ($h'F$ and $foF2$)
 85 and attributed them to the UFKWs simultaneously detected in the MLT region. G. Liu
 86 et al. (2012) examined global maps of total electron content (TEC) and incoherent scat-
 87 ter radar data during the UFKW event of January 2010. They suggested that the ob-
 88 served spatial and temporal features of the \sim 3 day variations in TEC and electron den-
 89 sity are consistent with the modulation of the equatorial plasma fountain by the UFKW.
 90 Phanikumar et al. (2014) observed TEC variations with UFKW periodicity (3–5 days)
 91 during January–February 2009 and associated them with the major sudden stratospheric
 92 warming (SSW) event that took place at this time. Gu et al. (2014) presented observa-
 93 tions of UFKWs in the temperature and zonal wind in the MLT region, and simultane-
 94 ously in global TEC maps and COSMIC electron density during the year 2011. They
 95 showed that there is a good correspondence between UFKW activity in the MLT region
 96 and that in the low-latitude ionosphere. Abdu et al. (2015) pointed out that the equa-
 97 torial vertical plasma drift velocity at post-sunset times sometimes exhibits \sim 3 day vari-
 98 ations during UFKW events in the MLT region.

99 Numerical models have been used to study excitation, dissipation, and propaga-
 100 tion characteristics of the UFKW. Forbes (2000) used a linear mechanistic model, in which
 101 UFKWs are generated through theoretical wave forcing (as predicted by classical wave
 102 theory) in the lower atmosphere. By running the model with the same wave forcing but
 103 with different background winds, it was demonstrated that the distribution of the zonal
 104 mean wind at the equator plays an important role for the UFKW propagation into the
 105 MLT region. Miyoshi and Fujiwara (2006), using a general circulation model (GCM),
 106 showed that the dissipation of UFKWs in the MLT region and accompanying momen-
 107 tum deposition into the mean flow can make a significant contribution to the intrasea-
 108 sonal variation of the zonal mean zonal wind in that region. Y.-W. Chen and Miyahara
 109 (2012) investigated fast and ultra-fast Kelvin waves generated in a GCM simulation. Both
 110 waves showed vertical propagation from the troposphere to higher altitudes, and they
 111 dissipate in the MLT region (\sim 60–80 km for the fast Kelvin waves and \sim 90–110 km for
 112 the UFKWs). Chang et al. (2010) used the NCAR Thermosphere Ionosphere Mesosphere

113 Electrodynamics General Circulation Model (TIME-GCM) to evaluate the impact of the
 114 UFKW on the thermosphere and ionosphere. Theoretical UFKW forcing was applied
 115 at the lower boundary of the model at \sim 30 km. Their results indicated thermospheric
 116 mass density perturbations of 8–12% at 350 km altitude and low-latitude TEC pertur-
 117 bations of 25–50% in response to the UFKW that has amplitude of 20–40 m/s in the zonal
 118 wind in the MLT region. They also clarified that the thermospheric response is due to
 119 the direct propagation of the wave into the upper thermosphere, while the ionospheric
 120 effects are caused by the modulation of the dynamo electric field. Onohara et al. (2013),
 121 using an ionospheric wind dynamo model, showed that \sim 3 day variations in the equa-
 122 torial vertical plasma drift velocity can be reproduced by forcing the model with a pa-
 123 rameterized UFKW and diurnal tide. Sassi et al. (2013), in their investigation of the Jan-
 124 uary 2009 SSW simulated by the Whole Atmosphere Community Climate Model eXtended
 125 version (WACCM-X), noted an enhancement of the UFKW in the MLT region during
 126 the SSW. Nystrom et al. (2018), based on a TIME-GCM simulation for April 2009, ex-
 127 plained how non-linear interactions between UFKWs and tides can lead to a rich wave
 128 spectrum in the MLT region. Triplett et al. (2019) used the TIE-GCM, which is sim-
 129 ilar to the TIME-GCM but with the lower boundary at \sim 97 km. The model was forced
 130 with a theoretical UFKW at the lower boundary, which was shown to produce TEC per-
 131 turbations of \pm 10% at low latitudes.

132 The present study also utilizes a numerical model to examine the UFKW in the
 133 middle and upper atmosphere. Specifically, we use the whole atmosphere model GAIA,
 134 which stands for Ground-to-topside model of Atmosphere and Ionosphere for Aeronomy.
 135 The main objectives of this study are to demonstrate model's ability to reproduce UFKW
 136 events that actually occurred in the real atmosphere and to understand the nature of
 137 the ionospheric variability caused by the wave activity. In many previous simulations,
 138 the UFKW was generated by artificial forcing inserted at a certain height with a fixed
 139 oscillation period and zonal wavenumber and with a latitudinal structure of perturba-
 140 tions predicted by linear wave theory (Forbes, 2000; Chang et al., 2010; Onohara et al.,
 141 2013; Triplett et al., 2019). An advantage of this approach is to be able to easily isolate
 142 the wave effects by switching on and off the forcing in the model, but the downside is
 143 that it is not possible to make a direct comparison with observations for any particu-
 144 lar event. Only a few numerical studies used realistic forcing based on meteorological data
 145 to drive the UFKW (Sassi et al., 2013; Nystrom et al., 2018). Sassi et al. (2013) were

able to reproduce the UFKW observed in the SABER temperature at 100 km altitude during January–February 2009. It needs to be remembered, however, that this was achieved by constraining the WACCM-X for the entire middle and lower atmosphere (0–90 km) with assimilation products. Nystrom et al. (2018) constrained the lower boundary of the TIME-GCM at \sim 30 km with meteorological reanalysis data for April 2009 and found marked UFKW activity in the MLT region at 90–150 km. However, they did not make a direct comparison with measurements. Therefore, it is uncertain at this point whether numerical models are capable of reproducing the UFKW in the MLT region in response to realistic forcing in the lower atmosphere. Besides, neither Sassi et al. (2013) nor Nystrom et al. (2018) investigated the ionospheric response, which still needs to be validated in the context of whole atmosphere modeling through direct comparisons with observations. This study addresses these issues by the use of the GAIA model and observational data from the middle atmosphere and ionosphere, which are described in the following section. Section 3 presents our results regarding the UFKW in the MLT region and ionosphere. The performance of the model is also evaluated therein. In section 4, we discuss the nature of the ionospheric variability during times of enhanced UFKW activity, based on a case study of the August–September 2011 event. Summary and conclusions are provided in section 5.

2 Model and Data

2.1 GAIA model

GAIA is a physics-based numerical model of the Earth's whole atmosphere (e.g., Jin et al., 2011; Miyoshi et al., 2011). The model simulates the dynamics, thermodynamics, chemistry, and electrodynamics of the coupled atmosphere-ionosphere system from the surface to the upper thermosphere/ionosphere. GAIA consists of three models that are coupled to one another: a whole atmosphere GCM (Miyoshi & Fujiwara, 2003), an ionosphere model (Shinagawa, 2011), and an electrodynamics model (Jin et al., 2008). The whole atmosphere GCM has the horizontal resolution 2.8° in longitude and latitude and the vertical resolution of a grid per 0.2 scale height, which is sufficient for resolving global-scale waves such as equatorial Kelvin waves and tides. The upper boundary is at 1.017×10^{-9} hPa, which corresponds to 480–620 km altitude in our simulations. The ionosphere model has the upper boundary at \sim 2,000 km altitude. The electron density is derived as a sum of the densities of O^+ , O_2^+ , N_2^+ , and NO^+ , and TEC is derived by

178 vertically integrating the electron density. The electrodynamics model solves a wind dy-
 179 namo equation to calculate electric fields and currents in a tilted dipole magnetic field
 180 configuration under the assumption of equipotential magnetic field lines.

181 The neutral atmosphere below 30 km is constrained with meteorological reanalysis
 182 data provided by the Japan Meteorological Agency (Onogi et al., 2007; Kobayashi
 183 et al., 2015) using a nudging technique similar to those used by Jin et al. (2012) and Miyoshi
 184 et al. (2017). In this way, the model takes into account wave forcing from the lower at-
 185 mosphere to the upper atmosphere including the ionosphere. The model also takes into
 186 account time-dependent forcing by energetic solar radiation. The daily $F_{10.7}$ index (Tapping,
 187 2013) is used as a proxy of the solar EUV/UV flux, which dominates heating and ion-
 188 ization processes in the upper atmosphere. Geomagnetically quiet conditions are real-
 189 ized by setting the cross polar cap potential to a low and constant value of 30 kV through-
 190 out the simulation. Therefore, the day-to-day variability in the model arises from me-
 191 teorological and solar radiation forcings but not from magnetospheric forcing.

192 A wave analysis was performed to identify UFKWs and other global-scale waves.
 193 At a given latitude, the amplitude A and phase ϕ of waves with period τ are expressed
 194 in the following formula:

$$195 \sum_{s=-4}^4 A_s \cos \left[\frac{\Omega}{\tau} t + s\lambda - \phi_s \right]. \quad (1)$$

196 Here Ω is the rotation rate of the Earth ($=2\pi/\text{day}$), t is the universal time (days), λ is
 197 the longitude (radians), and s is the zonal wavenumber. Waves with eastward and west-
 198 ward phase propagations correspond to $s < 0$ and $s > 0$, respectively, and zonally symmet-
 199 ric oscillations are $s = 0$. In the remainder of this paper, eastward- and westward-propagating
 200 waves with zonal wavenumber s are also referred to as $E|s|$ and $W|s|$, respectively. For
 201 example, the UFKW is eastward-propagating with zonal wavenumber $s = -1$ and hence
 202 an $E1$ wave. Standing oscillations are, in this case, denoted as $S0$. For each day, least-
 203 squares fitting was performed to GAIA data at a given latitude and height using time
 204 windows that are three times the wave period.

205 2.2 Geopotential height

206 The geopotential height (GPH) measurements from the Microwave Limb Sounder
 207 (MLS) aboard the Aura satellite (Waters et al., 2006; Schwartz et al., 2008) are used to
 208 identify UFKW events as well as to validate UFKWs reproduced by GAIA. Aura is NASA's

ongoing satellite mission. The spacecraft was launched into a sun-synchronous low Earth orbit on July 15, 2004. The Aura/MLS provides measurements of GPH profiles for pressure levels from 261 hPa (~ 9 km) to 0.001 hPa (~ 97 km). Version 4.2 data (Livesey et al., 2017) during 2004–2019 were obtained from the Goddard Earth Sciences Data and Information Services Center (Acker & Leptoukh, 2007). A wave analysis was performed in a similar way as described for GAIA. The reader is referred to Yamazaki and Matthias (2019) for the detailed description of how the Aura/MLS GPH data were processed for the wave analysis.

It is noted that since the Aura satellite is in a Sun-synchronous orbit, the measurements are limited to two local solar times at $\sim 1:45$ p.m. and $\sim 1:45$ a.m. Therefore, the wave analysis is based on the data at these local times, which contrasts to the wave analysis for GAIA that includes the data from all local times. Nevertheless, we found good agreement between the UFKW derived from GAIA GPH including all local times and that derived from GAIA GPH at local solar times of MLS measurements (i.e., $\sim 1:45$ p.m. and $\sim 1:45$ a.m.), indicating that the limited local-time coverage of Aura/MLS does not necessarily affect its ability to detect UFKWs. This justifies the comparison of UFKWs in GPH from Aura/MLS and GAIA (Section 3.1) despite the difference in local-time coverage.

2.3 Total electron content

TEC data from ESA's GOCE mission are used to evaluate UFKW effects in the ionosphere. The GOCE satellite was launched into a sun-synchronous low Earth orbit on 17 March 2009 and operated in the thermosphere at an altitude of ~ 250 km until October 2013. The slant TEC was derived from Global Positioning System (GPS) observations and then converted to the vertical TEC (Kervalishvili et al., 2018). The retrieval procedure is similar to that used earlier for deriving TEC from the GPS data for the CHAMP and Swarm satellites (e.g., Noja et al., 2013). A wave analysis was performed separately for the data from the ascending and descending orbital nodes, at ~ 7 p.m. and ~ 7 a.m. local solar time, respectively. This is because UFKW effects in the ionosphere are known to be local-time dependent (Gu et al., 2014). The wave analysis of GAIA TEC data was also performed separately at each local solar time. The resulting problem of aliasing will be discussed in 4.1. It is noted that GOCE TEC represents the vertical integration of the plasma density from the height of GOCE (~ 250 km) to the height of GPS satellites,

241 which differs from TEC measured at ground level. According to GAIA simulations, TEC
 242 at 250 km is lower than the ground TEC only by \sim 10%.

243 **2.4 Geomagnetic field**

244 Ground-based magnetometer data were obtained from five observatories: Huancayo (12.0°S, 75.3°W),
 245 Tatuoca (1.2°S, 48.5°W), Addis Ababa (9.0°N, 38.8°E), Tirunelveli (8.7°N, 77.8°E),
 246 Yap Island (9.3°N, 138.5°E). These observatories are longitudinally apart
 247 but they are all located near the magnetic equator (i.e., within \pm 3° magnetic latitudes).
 248 Magnetic data from Huancayo and Addis Ababa are provided through INTERMAGNET
 249 (Love & Chulliat, 2013), while Tirunelveli data are provided by the World Data Cen-
 250 ter (WDC) for Geomagnetism, Mumbai. The Tatuoca data are provided by Observatório
 251 Nacional (Morschhauser et al., 2017) and accessible from GFZ Data Services (Soares,
 252 Matzka, & Pinheiro, 2018). The magnetometer at Yap Island belongs to the global mag-
 253 netometer network MAGDAS (Yumoto & the MAGDAS Group, 2006) and the data are
 254 accessible through SuperMAG (Gjerloev, 2012).

255 For each station, the magnetic northward (N) component of the geomagnetic field
 256 was derived through a coordinate conversion. The data were corrected for magnetic dis-
 257 turbances associated with large-scale magnetospheric currents, such as the ring current
 258 and magnetotail current (e.g., Lühr et al., 2017). The correction was performed by sub-
 259 tracting the external field obtained from the magnetic field model CHAOS-6 (Finlay et
 260 al., 2016). Furthermore, quiet-day nighttime values were subtracted from the time se-
 261 ries of N for each station, which removes the magnetic fields originating from the Earth's
 262 core and lithosphere. The residual field Δ N represents magnetic perturbations produced
 263 by electric currents in the ionosphere. Since the observatories are close to the magnetic
 264 equator, Δ N is dominated by the effect of the equatorial electrojet, which is a narrow
 265 band of a zonal current along the magnetic equator (e.g., Yamazaki & Maute, 2017). The
 266 equatorial electrojet is closely associated with the equatorial zonal electric field gener-
 267 ated through wind dynamo processes in the ionospheric E region (e.g., Alken, 2020).

268 **3 Results**

269 **3.1 UFKWs in the MLT region**

270 Figure 1 shows the amplitude of the UFKW in GPH at 0.001 hPa (~ 97 km) in the
 271 lower thermosphere during 2004–2019. The UFKW amplitude here is defined as the largest
 272 amplitude of the E1 waves within periods of 2.25–3.75 days. The amplitude tends to be
 273 largest over the equator and its latitudinal structure is symmetric about the equator. These
 274 features are consistent with those reported earlier by G. Liu et al. (2019) based on SABER
 275 temperature data at 110 km during 2002–2018. There are occasionally bursts of wave
 276 activity with amplitudes exceeding 0.2 km at the equator, which is appreciably larger
 277 than the typical 1σ error in the amplitude (< 0.05 km) estimated by Yamazaki and Matthias
 278 (2019). In what follows, we validate the performance of GAIA in reproducing UFKWs
 279 in the MLT region. Our focus is on these three events that involve particularly strong
 280 UFKW activity: (1) September 2010, (2) August–September 2011, and (3) December
 281 2012–January 2013.

282 Figure 2 presents wave spectra from $s = -2$ to $s = +2$ at 0.001 hPa (~ 97 km) over
 283 the equator during the September 2010 event. The left panel is derived from the Aura/MLS
 284 observations while the right panel is from GAIA simulations. Enhanced wave activity
 285 is seen throughout September 2010 for E1 waves with a period around 2.5 days, which
 286 can be identified as UFKWs. Other spectral components are mostly on the background
 287 level below 0.1 km, except there is some W1 wave activity with a period of 4–7 days at
 288 end of August, which is likely due to the Rossby normal mode, the so-called quasi-6-day
 289 wave (e.g., Gan et al., 2018; Gu, Ruan, et al., 2018). In Figures 3 and 4, wave spectra
 290 are plotted in a similar format as Figure 2 but for the August–September 2011 event and
 291 the December 2012–January 2013 event, respectively. In either case, the GAIA repro-
 292 duces the temporal variation of UFKW activity well but with slightly lower amplitudes.

293 Figures 5a–5d compare the vertical structures of the observed and simulated UFKWs
 294 during the August–September 2011 event. The amplitude and phase are derived for the
 295 E1 wave with a period of 3.0 days. The GAIA captures the height growth and latitu-
 296 dinal spread of the UFKW amplitude well. The phase structure of the UFKW in the MLT
 297 region (above 1 hPa) is also well reproduced by GAIA. Similarly good agreement is ob-
 298 tained between the Aura/MLS observations and GAIA simulations for the September
 299 2010 event and the December 2012–January 2013 event. Figures 5e–5h show the model-

300 data comparisons of the UFKW amplitudes for these events. It is noted that the December
 301 2012–January 2013 event involves three discrete bursts of UFKW activity (Figure
 302 4) and in Figures 5g and 5h we highlight only the event of 7–15 January 2013, in which
 303 GAIA shows the largest wave activity. The model-data comparisons of the UFKW phase
 304 for the September 2010 event and the December 2012–January 2013 event are presented
 305 in the supporting information (Figure S1).

306 3.2 UFKWs in the thermosphere

307 Since the GAIA model is shown to be able to reproduce UFKW activity in the MLT
 308 region, which is well above the region constrained by meteorological reanalysis data (0–
 309 30 km), we now use GAIA to investigate the UFKW activity for the entire atmosphere.
 310 Figure 6 shows the amplitude and phase of the UFKW in the zonal wind (a, b), merid-
 311 ional wind (c, d), and temperature (e, f) for the August–September 2011 event. UFKW
 312 amplitudes in the zonal wind greater than 10 m/s are mainly confined within a latitude
 313 range of $\pm 30^\circ$ and an altitude range of 85–150 km. The peak amplitude of 35 m/s is found
 314 at 103 km altitude near the equator. Amplitudes in the meridional wind are relatively
 315 small, with the maximum value less than 10 m/s. The amplitude in the temperature reaches
 316 its maximum value of 14 K at 111 km altitude near the equator. Compared to the zonal
 317 wind amplitude, the temperature amplitude decays slowly with height above the ampli-
 318 tude peak. Gu et al. (2014) reported an amplitude of ~ 30 m/s in the zonal wind at 90–
 319 100 km altitude and 15 K in the temperature at 100–104 km altitude for the same event
 320 based on TIMED satellite measurements, which is in agreement with the GAIA results.

321 In the low-latitude MLT region, UFKW phases in the zonal wind and temperature
 322 tend to be horizontally uniform and they show a downward phase propagation, which
 323 is consistent with the upward energy propagation. The vertical wavelength is ~ 40 km
 324 for the altitude range of 60–110 km for both the zonal wind and temperature, which is
 325 in agreement with earlier observations (e.g., Davis et al., 2012). In the upper thermo-
 326 sphere, above 200 km or so, the phases are largely independent of height. The UFKW
 327 phase in the meridional wind shows a complex pattern in the low and middle atmosphere
 328 due to the small amplitude. In the upper thermosphere, the meridional wind phase is
 329 anti-symmetric about the equator.

The vertical and horizontal structures of the UFKW in the zonal wind, meridional wind and temperature presented in Figures 6a–6f are in good agreement with those by Chang et al. (2010) for an idealized TIME-GCM simulation. Similar results are obtained for the September 2010 event and the December 2012–January 2013 event. The UFKW amplitudes in the zonal wind are presented in Figures 6g and 6h for these events. In both cases, the maximum amplitude in the zonal wind exceeds 30 m/s in the MLT region at the equator. Given that the GAIA model tends to underestimate the amplitude in the geopotential height in the MLT region (Figures 2–4), the actual zonal wind amplitude could be larger. In Figures S2 and S3 of the supporting information, we plot the amplitudes and phases of the UFKW in the zonal wind, meridional wind, and temperature for the September 2010 event and the December 2012–January 2013 event.

3.3 Ionospheric variability during UFKW events

We now turn our attention to the response of the ionosphere to the UFKW. GAIA’s capability to reproduce the ionospheric response is verified through comparisons between observed and simulated UFKWs in the ionosphere. Ionospheric variability associated with the UFKW may be extracted from parameters such as TEC and equatorial zonal electric field (EEF) using the formula (1). However, unlike the neutral atmosphere, the response of the ionosphere to the UFKW is highly dependent on local solar time (e.g., Chang et al., 2010; Gu et al., 2014). Therefore, fitting of (1) to observational and model data is performed at a fixed local solar time. In the following, we present the spectral component corresponding to the UFKW ($s=-1$, $\tau\sim 3$) in the ionosphere, as derived from the GOCE TEC observations and GAIA simulations, during the August–September 2011 event and the December 2012–January 2013 event. Unfortunately, there is a large gap in the GOCE data during the September 2010 event, and thus our analysis is limited to the other two events.

Figure 7 compares the UFKW spectral component in TEC observed by the GOCE satellite and simulated by the GAIA model during the August–September 2011 event. It is noted that in Figure 7, different color scales are adopted for different panels. The top panels (Figures 7a and 7b) present the background TEC at 7 p.m. local solar time, which corresponds to the ascending node of the GOCE orbit. These TEC values are calculated as the zonal and temporal mean within a 9-day moving window, which is also the time window used for calculating the amplitudes of the UFKW spectral component

in Figures 7c–7f. In both the GOCE and GAIA results, the background TEC has a local maximum on both sides of the magnetic equator, reflecting the equatorial ionization anomaly (EIA) structure that is usually formed during the daytime due to the equatorial plasma fountain effect. The background TEC in GAIA is somewhat higher than that in GOCE observations, and also the EIA crests are located at higher latitudes in GAIA than those derived from GOCE data. This could be due to an overestimation of the daytime equatorial zonal electric field in GAIA, in other words, an overestimation of the equatorial plasma fountain effect. It is seen in Figures 7c and 7d that the amplitude of the UFKW spectral component in TEC also exhibits a double-peak structure. Local maxima of the amplitude occur at poleward edges of the EIA crests. The maximum amplitudes are ~ 8 TECU in the GOCE data and ~ 6 TECU in the GAIA model, which correspond to $\sim 30\%$ and $\sim 20\%$ of the background TEC, respectively (see Figures 7e and 7f).

Figure 8 presents model-data comparisons for the December 2012–January 2013 event. The maximum amplitudes are, again, ~ 8 TECU ($\sim 30\%$) in the GOCE data and ~ 6 TECU ($\sim 20\%$) in the GAIA model, occurring at poleward edges of the EIA crests. The GOCE observations suggest that the ionospheric response is strongest around 5–10 February 2013, while in GAIA, the ionospheric response is more pronounced from end of December 2012 towards early January. This discrepancy can be attributed to the underestimation of UFKW forcing during early February 2013 (see Figure 4).

It is noted that there was an SSW event in January 2013 (Goncharenko et al., 2013). The central date of the SSW was on 7 January (Siddiqui et al., 2018) and associated ionospheric perturbations have been observed in the following days (Goncharenko et al., 2013; Jonah et al., 2014). This coincides with the period of enhanced UFKW activity in the middle atmosphere (Figure 4) and ionosphere (Figure 9). However, it is unclear if the UFKW event in January 2013 is related to the SSW, as UFKW bursts are also observed before and after the SSW. The relationship between SSW and UFKW is still under debate (e.g., England et al., 2012; G. Liu et al., 2012; Sassi et al., 2013; Phanikumar et al., 2014).

Figure 9 is the same as Figure 7 but for 7 a.m. local solar time, which corresponds to the descending node of the GOCE orbit. The GOCE TEC data reveal an enhancement in the amplitude of the UFKW spectral component at $0\text{--}20^\circ$ magnetic latitudes

394 during 30 August–7 September 2011. This coincides with the time of enhanced UFKW
 395 activity observed in the ascending node. The absolute amplitude is small (~ 1.5 TECU
 396 at maximum) but the relative amplitude exceeds 10% of the background TEC. The GAIA
 397 does not reproduce the ionospheric response at this local solar time, possibly because
 398 of the underestimation of UFKW forcing in the model. Similarly, enhanced UFKW ac-
 399 tivity (~ 1.5 TEC, $\sim 10\%$) was observed in the descending node during 29 January–10
 400 February 2013, and the GAIA model did not reproduce the observation (Figure 4S in
 401 the supporting information).

402 Gu et al. (2014) analyzed global TEC maps derived from ground GPS data and
 403 investigated UFKW signatures during 2011. They showed the dependence of UFKW sig-
 404 natures in TEC on local solar time and magnetic latitude around the time of the August–
 405 September 2011 event, which gives us the opportunity to further validate the GAIA re-
 406 sults. We show in Figures 10a and 10c the local solar time and magnetic latitude depen-
 407 dence of the background TEC and the amplitude of the UFKW spectral component in
 408 TEC during 27 August–4 September 2011. Therein, the TEC values are evaluated at the
 409 ground level, not at 250 km altitude as in Figures 7–9. Our results are in good agree-
 410 ment with those presented by Gu et al. (2014) (see their Figures 5c and 5d).

411 Gu et al. (2014) also presented the dependence of the UFKW amplitude in the elec-
 412 tron density (N_e) on magnetic latitude and on altitude using COSMIC data during 8–
 413 22 February 2011. In Figures 10b and 10d, we show similar results but for the August–
 414 September 2011 event. Despite the difference in the time intervals examined, our results
 415 agree qualitatively with those by Gu et al. (2014) (see their Figures 6a and 6b). In both
 416 results, the UFKW amplitude in N_e show local maxima at the poleward and equator-
 417 ward edges of the EIA crests. This can be understood as a consequence of the equato-
 418 rial plasma fountain effect. That is, when an eastward dynamo electric field is imposed
 419 on the dayside ionosphere, not only the electron density at the EIA crests increases but
 420 also the location of the EIA crests moves poleward (Stolle et al., 2008). Thus, as the zonal
 421 electric field oscillates due to the UFKW, largest perturbations in the electron density
 422 tend to occur where the density gradient is most significant, which is not at the EIA crests
 423 but at their poleward and equatorward edges.

424 Figures 11a and 11b compare the spectra for the observed and simulated TEC at
 425 7 p.m. local solar time at 250 km altitude near the northern EIA crest during the August–

September 2011 event. In both cases, a spectral peak is visible at $s=-1$ and a period of ~ 3 days. A similar peak is found in the spectra for the daytime equatorial zonal electric field at 110 km (Figure 11c) and for the equatorial zonal wind at the same height (Figure 11d). These results suggest that the equatorial zonal electric field is modulated by the zonal wind, and subsequently the plasma distribution in the EIA region is modulated by the equatorial zonal electric field. As demonstrated by Yamazaki et al. (2014), the zonal wind at 100–120 km altitude in the equatorial region is effective in perturbing the dayside zonal electric field. The UFKW amplitude in the zonal wind happens to be largest in that region (Figure 6), allowing the UFKW to efficiently drive ionospheric variability. In Figure 11c, the spectra for the equatorial zonal electric field are computed using only the daytime data between 7 a.m. and 5 p.m. local solar time. This is because the response of the equatorial zonal electric field to the zonal wind is different during daytime and nighttime (Jin et al., 2008). Indeed, spectral patterns are different for daytime and nighttime equatorial zonal electric fields, although zonal wind spectra are consistent between daytime and nighttime. This is demonstrated in the supporting information (Figure S5).

4 Discussion

In the previous section, we have validated GAIA’s ability to reproduce ionospheric variability during UFKW events. In this section, we will investigate the simulated UFKW signatures in the ionosphere during the August–September 2011 event in more detail. We first discuss potential aliasing from other waves and tides into the UFKW spectrum component (i.e., $s=-1$ and $\tau \sim 3$ days) in the ionosphere. We then discuss the nature of the ionospheric variability during the UFKW event and possible detection of UFKW signatures using ground-based measurements. To facilitate the discussion, we have performed two numerical experiments as summarized in Table 1. In these numerical experiments, the neutral component of GAIA is de-coupled from the ionospheric and electrodynamics models. The atmospheric temperature, winds, and composition are analyzed using the Fourier transform and reconstructed with the wave components having zonal wavenumbers from $s=-5$ to $s=+5$ only. In the first experiment “LARGE_WAVES”, the ionospheric and electrodynamics models are forced with the reconstructed neutral fields. The main difference between the original GAIA simulation and LARGE_WAVES is that GAIA includes the waves that have relatively small spatial scales ($s > +5$ and $s < -5$), which are

458 excluded in LARGE_WAVES. Also, GAIA takes into account the feedback process from
 459 the ionosphere to the neutral atmosphere, which is ignored in LARGE_WAVES. The sec-
 460 ond experiment “NO_UFKW” is the same as LARGE_WAVES but the E1 waves at pe-
 461 riods 1.5–4.5 days are removed using the method of (Hayashi, 1971). This eliminates the
 462 UKFW in the neutral atmosphere and its direct influence on the ionosphere.

463 **4.1 Aliasing**

464 In Section 3.3, the ionospheric variability associated with the UKFW was eval-
 465 uated by fitting the formula (1) to GOCE and GAIA TEC at a fixed local solar time. These
 466 fits can suffer from aliasing with various combinations of zonal wavenumber s and pe-
 467 riod τ . Here we discuss and identify potential sources of aliasing, and later we will make
 468 an attempt to separate the aliasing sources from UKFW signatures in the ionosphere based
 469 on the controlled simulations, LARGE_WAVES and NO_UFKW.

470 Using the local solar time t_{LT} ($=t + \frac{\lambda}{\Omega}$), a wave $\cos(\frac{\Omega}{\tau}t + s\lambda)$ can be expressed
 471 as

$$472 \cos \left[\left(s - \frac{1}{\tau} \right) \lambda + \frac{\Omega}{\tau} t_{LT} \right]. \quad (2)$$

473 At a fixed local solar time, $\frac{\Omega}{\tau}t_{LT}$ is a constant, and thus (2) is a function of longitude.
 474 In principle, the waves that have the same longitudinal dependence are indistin-
 475 guishable. For the UKFW, $s=s_u$ ($=-1$) and $\tau=\tau_u$ (~ 3), and one cannot distinguish the UKFW
 476 from other waves that satisfy:

$$477 |s - \frac{1}{\tau}| = s_u - \frac{1}{\tau_u}. \quad (3)$$

478 For global-scale waves, zonal wavenumber s needs to be an integer and period τ needs
 479 to be positive. Under these restrictions, there is a series of combinations (s, τ) that sat-
 480 isfy (3). Table 2 lists combinations (s, τ) for the waves from which aliasing can occur
 481 into the UKFW spectral component ($s_u=-1, \tau_u=2-4$ d) at a fixed local solar time. As
 482 it turns out, τ is negative if $s < 0$, so that aliasing does not occur from eastward-propagating
 483 waves. For $s \geq 0$, τ is mostly less than one day. The only wave with $\tau \geq 1.0$ d is $s=+2$ and
 484 $\tau=1.33-2.00$ d. The mixed Rossby-gravity wave, also known as the quasi-2-day wave, is
 485 westward-propagating with $s=+2$, $s=+3$, or $s=+4$ (e.g., Gu, Dou, et al., 2018), and thus
 486 the $s=+2$ component is a potential source of aliasing. In general, quasi-2-day waves are
 487 strongest in the summer hemisphere. The $s=+2$ component in the MLT region attains

its maximum amplitude in early August in the Northern Hemisphere and in mid November in the Southern Hemisphere (Pancheva et al., 2018).

None of the waves in Table 2 has an overlap with tidal periodicities ($\tau=1\text{d}$, $\frac{1}{2}\text{d}$, $\frac{1}{3}\text{d}$, $\frac{1}{4}\text{d}$), thus aliasing from tidal waves do no occur as long as their amplitudes and phases stay constant. However, tides in the MLT region are known to be highly variable, and their amplitudes and phases can change significantly from one day to the next (e.g., Miyoshi & Fujiwara, 2003; Fang et al., 2013). Short-term tidal variability will inevitably contribute to the spectral components listed in Table 2. One of the causes of day-to-day tidal variability is the non-linear interaction between tides and other waves, which generate secondary waves at periods close to tidal periodicities and hence modulate the tides (e.g., Chang et al., 2011; Pedatella et al., 2012). In the following, we consider aliasing by the waves generated through the non-linear interaction of the UFKW and tides.

According to the theory of Teitelbaum and Vial (1991), the non-linear interaction of two global-scale waves can give rise to secondary waves with frequencies and zonal wavenumbers that are the sums and differences of those of the interacting waves. Thus, the non-linear interaction between an UFKW $\cos\left(\frac{\Omega}{\tau_u}t + s_u\right)$ and tidal wave $\cos(n\Omega t + s\lambda)$ leads to secondary waves:

$$\cos\left[\left(\frac{\Omega}{\tau_u} \pm n\Omega\right)t + (s_u \pm s)\lambda\right], \quad (4)$$

where $n=1, 2, 3$ represent oscillations with periods corresponding to 1d (diurnal tide), $\frac{1}{2}\text{d}$ (semidiurnal tide), and $\frac{1}{3}\text{d}$ (terdiurnal tide), respectively. In the local-time frame, this becomes:

$$\cos\left[\left(s_u \pm s - \frac{1}{\tau_u} \mp n\right)\lambda + \left(\frac{\Omega}{\tau_u} \pm n\Omega\right)t_{LT}\right], \quad (5)$$

Therefore, at a fixed local solar time, aliasing into the UFKW (s_u, τ_u) occurs if

$$|s_u \pm s - \frac{1}{\tau_u} \mp n| = s_u - \frac{1}{\tau_u}. \quad (6)$$

Since s and n are required to be an integer and a natural number, respectively, the only possible solution is:

$$n = s, \quad (7)$$

that is, migrating tides. In other words, secondary waves generated by the non-linear interaction of the UFKW and migrating tides cannot be distinguished from the UFKW when the wave signatures are sampled at a fixed local solar time. For example, the non-linear interaction between the UFKW ($s=-1, \tau=3\text{d}$) and migrating diurnal tide ($s=+1,$

519 $\tau=1\text{d}$) leads to secondary waves with ($s=0$, $\tau=0.75\text{d}$) and ($s=+2$, $\tau=1.5\text{d}$), both of which
 520 can be found in Table 2. In fact, for each wave in Table 2, it is possible to find a pair
 521 of the UFKW and migrating tide that can be a potential source of aliasing.

522 Aliasing effects are expected to reduce when the wave signatures are sampled over
 523 a range of local solar time instead of a single local solar time. To confirm this, we gen-
 524 erated synthetic data by sampling the waves listed in Table 2 over a range of local so-
 525 lar time (e.g., 9 a.m.–3 p.m.). The amplitude of the UFKW spectral component ($s=-1$,
 526 $\tau=3\text{d}$) was calculated by fitting (1) to the synthetic data. The derived amplitude is com-
 527 compared with that calculated with the synthetic data sampled at a fixed local solar time
 528 (e.g., 12 noon). The amplitude ratio γ is listed in Table 2 for ranges of local solar time
 529 3h, 6h, and 12h. As expected, aliasing effects are smaller when the data from a wider
 530 range of local solar time are included in the wave analysis. For instance, aliasing from
 531 the wave ($s=+1$, $\tau=0.40\text{--}0.44\text{d}$) can be largely avoided, if the data are included for the
 532 whole daytime period, which corresponds to a local-time range of 12h.

533 The controlled simulations, LARGE_WAVES and NO_UFKW, help us understand
 534 aliasing effects in the UFKW spectral component that we presented in Section 3.3. Fig-
 535 ure 12a is the same as Figure 11d but derived from LARGE_WAVES, showing the zonal
 536 wavenumber spectrum of the equatorial zonal wind at 110 km during the August–September
 537 2011 event. It is noted that the wave analysis includes the zonal wind data from all lo-
 538 cal solar times. The results from GAIA (Figure 11d) and LARGE_WAVES (Figure 12a)
 539 are almost identical, indicating that the feedback effect from the ionosphere to the neu-
 540 tral atmosphere, which is taken into account in GAIA but not in LARGE_WAVES, does
 541 not play a significant role for global-scale waves at 110 km. Figure 12b shows the spec-
 542 trum derived from NO_UFKW, which eliminates the E1 waves with periods ~ 3 days.
 543 The spectral pattern is consistent with that of LARGE_WAVES in Figure 12a except
 544 for the absence of the UFKW.

545 Figure 12c presents the zonal wavenumber spectrum of the equatorial zonal elec-
 546 tric field as derived from LARGE_WAVES. It is noted that the only daytime data (7 a.m.–
 547 5 p.m.) are included in the wave analysis. The result shows a spectral peak at $s=-1$ and
 548 $\tau\sim 3\text{d}$, in good agreement with the GAIA simulation (Figure 11c). In the NO_UFKW
 549 run (Figure 12d), the spectral peak is reduced below the 95% confidence level. These re-

550 sults suggest that the spectral peak in the daytime equatorial zonal electric field at $s=-1$
 551 and $\tau \sim 3$ d during the August–September 2011 event is directly caused by the UFKW.

552 Figures 12e and 12f show zonal wavenumber spectra of TEC at 7 p.m. local solar
 553 time as derived from LARGE_WAVES and NO_UFKW, respectively. The LARGE_WAVES
 554 simulation case reveals enhanced wave activity at $s=-1$ and $\tau \sim 3$ d, which is consistent
 555 with the GAIA result (Figure 11b) as well as GOCE observation (Figure 11a). It is in-
 556 teresting to note that wave activity at $s=-1$ and $\tau \sim 3$ d is also seen in NO_UFKW, which
 557 excludes forcing by the UFKW. There are at least three significant peaks in the E1 spec-
 558 trum at periods 2–4 days. Each peak has a spectral amplitude ~ 1.8 TEC, which is about
 559 half the amplitude of the UFKW spectral component in LARGE_WAVE (~ 4 TEC). These
 560 spectral peaks in NO_UFKW TEC are due to aliasing from westward-propagating waves
 561 with $\tau \leq 2.0$ d as listed in Table 2. These results suggest that UFKW activity in the iono-
 562 sphere observed at a fixed local solar time is contributed not only by the UFKW but also
 563 by other waves, such as secondary waves due to the non-linear interaction between the
 564 UFKW and migrating tides as discussed earlier.

565 4.2 Ground observer perspective

566 Up to now, we have mainly considered the ionospheric response to the UFKW from
 567 a perspective of the GOCE satellite at a fixed local solar time. We now discuss the wave
 568 effect from a ground observer perspective. For a ground observer at a fixed geograph-
 569 ical location, the UFKW manifests as a ~ 3 -day oscillation of atmospheric parameters.
 570 Therefore, the question is whether the ~ 3 -day variation caused by the UFKW is sub-
 571 stantially larger than ~ 3 -day variations due to other causes.

572 Figure 13a depicts the temporal and longitudinal variations of the equatorial zonal
 573 wind at 110 km during 15 August–20 September 2011 as derived from the LARGE_WAVES
 574 simulation. A 24h average was applied to the wind data at each longitude in order to
 575 suppress the variations associated with tides with periods less than one day. The zonal
 576 wind shows large day-to-day variability about ± 60 m/s. There is a hint of E1 wave ac-
 577 tivity with a period of ~ 3 days from end of August towards beginning of September. Fig-
 578 ure 13d is the same as Figure 13a but a bandpass filter is applied at each longitude to
 579 extract the variations with periods 1.5–4.5 days. Enhanced E1 wave activity is more clearly
 580 visible. Figure 13g presents the corresponding result from the NO_UFKW simulation,

which does not include E1 waves with periods of 1.5–4.5 days. In this case, ∼3-day variability can arise from ∼3-day waves with other zonal wavenumbers (i.e., W5–W1, S0, E2–E5) as well as from secondary waves due to the non-linear interaction between tides and ∼3-day waves. In Figure 13g, ∼3-day variability is much weaker than in Figure 13d, indicating that the UFKW is the leading cause of ∼3-day variations for a ground observer at a fixed longitude. Similar results were obtained for equatorial zonal winds at lower altitudes in the MLT region (not shown here). Thus, it is possible to detect UFKW signatures using a ground-based instrument such as a meteor radar (e.g., Vincent, 1993).

The results are presented in a similar format for the equatorial zonal electric field at 110 km in Figures 13b, 13e, 13h, and 13k, and for TEC at 20° magnetic latitude in Figures 13c, 13f, 13i, and 13l. For these ionospheric parameters, the contributions of the UFKW (Figures 13h and 13i) and non-UFKW sources (Figures 13k and 13l) are comparable, and the relative contribution of the two depends on longitude. The ∼3-day variations due to the UFKW and other sources could strengthen or cancel each other depending on their phases. Thus, a ground observer does not necessarily detect enhanced ∼3-day ionospheric variability even during times of enhanced UFKW activity. The same conclusion was reached when the ionospheric parameters at a fixed local solar time were analyzed at each longitude. Figure S6 in the supporting information shows plots similar to those in Figure 13 but derived using the equatorial zonal electric field at 12 noon local solar time and TEC at 7 p.m. local solar time.

It may be noted in Figures 13k and 13l that the amplitude of ∼3-day ionospheric variations caused by the UFKW depends on longitude. This is, in part, due to the longitudinal variation of the geomagnetic field. The Earth's main magnetic field plays an important role for the ionospheric electrodynamics (Takeda, 1996; Cnossen & Richmond, 2013) and its zonal structure can be imprinted in ionospheric parameters (Yue et al., 2013). Since the GAIA model assumes a simple dipole magnetic field that is tilted against the Earth rotation axis, the longitudinal asymmetry of ionospheric variations associated with the UFKW could be more pronounced in the real geomagnetic field configuration.

4.3 Ground-based magnetometer detection of the UFKW

The results presented above suggest that during times of high UFKW activity, an enhancement occurs in the spectral component of the ionospheric variability correspond-

612 ing to the UFKW (i.e., period $\tau \sim 3$ days and zonal wavenumber $s=-1$) (Figures 11 and
 613 12) but this does not necessarily lead to an enhancement in ~ 3 -day ionospheric varia-
 614 tions at a fixed longitude due to the presence of other ~ 3 -day variability (Figure 13).
 615 Keeping this in mind, we examine ground-based magnetometer data during the UFKW
 616 event of August–September 2011 and discuss the possible detection of UFKW signatures.

617 Figure 14a shows the distribution of the ground-based magnetometers used in this
 618 study. As mentioned earlier, these five observatories are all located in the vicinity of the
 619 magnetic equator, and thus the magnetic perturbations in the magnetic-northward com-
 620 ponent (ΔN) are predominantly due to the equatorial electrojet, which is closely asso-
 621 ciated with the equatorial zonal electric field. Examples of ΔN data are plotted in Fig-
 622 ure 14b for Huancayo and Addis Ababa. In general, ΔN is very small at night because
 623 of the absence of the equatorial electrojet due to low ionospheric conductivities, and ΔN
 624 is usually positive during the day, reflecting the eastward current flow of the equatorial
 625 electrojet, with a daily maximum around 11 a.m. local solar time. The daily maximum
 626 values exhibit day-to-day variability, which is mostly due to day-to-day variations of the
 627 equatorial zonal electric field (Yamazaki et al., 2018).

628 Figures 14c–14g show wavelet power spectra of ΔN at different locations. The wavelet
 629 analysis is based on the technique detailed by Torrence and Compo (1998). A similar
 630 method has been used in previous studies to examine spectral features of the equatorial
 631 electrojet and discuss their possible connections with atmospheric waves (e.g., Jarvis,
 632 2006; Ramkumar et al., 2009; Gurubaran et al., 2011). In our wavelet analysis, the data
 633 are included for both daytime and night time. The results are similar when the night
 634 time data are excluded. The wavelet spectrum of ΔN at Huancayo (Figure 14d) reveals
 635 the presence of relatively large ~ 3 -day variations from end of August to beginning of Septem-
 636 ber 2011. The spectrum at the closest observatory, Tatuoca (Figure 14f), shows a sim-
 637 ilar pattern but with maximum activity of ~ 3 -day variations on 2 September slightly later
 638 than that at Huancayo on 31 August. Although the two observatories are less than 30°
 639 apart in longitude, the behavior of the equatorial electrojet could be different as discussed
 640 in detail by Soares, Yamazaki, et al. (2018). In both Huancayo and Tatuoca results, there
 641 is a broader spectral peak at 5–10 days. Evidence suggests that geomagnetic activity is
 642 responsible for these variations. In Figure 14h, the wavelet spectrum is presented for the
 643 geomagnetic activity index K_p . The spectral peak around 5–10 days is visible from end
 644 of August 2011 for the rest of the period. It is known that the equatorial electrojet varies

with geomagnetic activity (e.g., Yamazaki & Kosch, 2015; Xiong et al., 2016). The equatorial electrojet is also known to vary with solar activity (e.g., Matzka et al., 2017). We plot the wavelet spectrum of the solar activity index $F_{10.7}$ in Figure 14i. On the time scale of our interest, variations of $F_{10.7}$ are mainly at the period of the solar rotation and its harmonics (27, 13.5, and 9 days) and thus would make little contribution to \sim 3-day variations of the equatorial electrojet. The wavelet spectra of ΔN for Addis Ababa, Tirunelveli, and Yap Island are presented in Figures 14c, 14e and 14g, respectively. They are only in partial agreement with one another and with those for Huancayo (Figure 14d) and Tatuoca (Figure 14f). For instance, at Addis Ababa (Figure 14c), \sim 3-day and 5–10 day variations, which are identified in the Huancayo and Tatuoca data, are barely visible in the wavelet spectrum. The lack of the 5–10 day variations can arise from the fact that the response of the equatorial electrojet to geomagnetic activity varies with longitude because of local-time differences (e.g., Maute et al., 2015). At Tirunelveli (Figures 14e) and Yap Island (Figures 14g), variations at a period of 2–3 days are seen in wavelet spectra but they occur a few days after those at Huancayo and Tatuoca. These discrepancies highlight the difficulty to confidently identify the UFKW activity from the magnetic data obtained at a single location.

Next, the zonal wavenumber spectrum is derived by fitting the formula (1) to the daytime ΔN data at the five observatories. The zonal wavenumbers only from -3 to $+3$ are considered due to the limited longitudinal coverage of the stations (Figure 14a). The result presented in Figure 14j reveals a significant peak at periods 2.5–3 days with zonal wavenumber $s=-1$. This is consistent with the result for the daytime equatorial zonal electric field derived from the GAIA model (Figure 11c). We showed earlier that this spectral peak is directly caused by the UFKW based on controlled simulations (Figures 12c and 12d). This is the first time that magnetic signatures of the UFKW in the equatorial electrojet are detected. It supports our hypothesis from the numerical experiments that UFKW activity leads to an enhancement of the spectral component in the ionosphere with period $\tau \sim 3$ days and zonal wavenumber $s=-1$, although \sim 3-day variations are not necessarily observed at a fixed longitude. This underlines the importance of multipoint measurements when UFKW signatures in the ionosphere are investigated using ground-based observations. A multipoint-measurement approach was used in the past in attempts to observe ionospheric signatures associated with the quasi-2-day wave, quasi-6-day wave,

677 and fast Kelvin wave from the ground (Pancheva et al., 2006, 2008). Our results sup-
 678 port such an approach for studying the UFKW.

679 5 Summary and Conclusions

680 In this study, we use the whole atmosphere model GAIA to simulate equatorial Kelvin
 681 waves with a period of ~ 3 days, also known as ultra-fast Kelvin waves (UFKWs). We
 682 examine the UFKW events of September 2010, August–September 2011, and December
 683 2012–January 2013, which are particularly strong according to the 16 years of geopoten-
 684 tial height measurements by the Aura Microwave Limb Sounder (MLS) (Figure 1). As
 685 we constrain the lower layers of GAIA below 30 km with meteorological reanalysis data,
 686 the model is able to reproduce main characteristics of UKFWs in the mesosphere and
 687 lower thermosphere (MLT) region as observed by the Aura/MLS (Figures 2–5). Accord-
 688 ing to the GAIA results, the zonal wind amplitude exceeds 30 m/s in the lower thermo-
 689 sphere (95–110 km) during these events (Figure 6), which is consistent with the earlier
 690 observations by Gu et al. (2014) during the August–September 2011 event.

691 GAIA is also able to reproduce wave activity in the total electron content (TEC)
 692 retrieved from GPS observations by the GOCE satellite at ~ 7 p.m. local solar time (Fig-
 693 ures 7 and 8). The GOCE data reveal the amplitude of the UFKW spectral component
 694 being up to 8 TECU (30% of the background) at $\pm 15^\circ$ magnetic latitudes, while the model
 695 data show the smaller amplitude up to 6 TECU (20% of the background) at $\pm 20^\circ$ mag-
 696 netic latitudes. The GOCE data also show the wave activity at ~ 7 a.m. local solar time
 697 with the amplitude up to 1.5 TECU (10% of the background), which the GAIA model
 698 does not capture well (Figure 9). The dependence of the amplitude of the UFKW spec-
 699 tral component in TEC on magnetic latitude, local solar time, and altitude during the
 700 August–September 2011 event (Figure 10) is consistent with the earlier report by Gu et
 701 al. (2014). The TEC response to the UFKW can be explained by the modulation of the
 702 equatorial zonal electric field (and thus the equatorial plasma fountain) by the zonal wind
 703 (Figure 11), confirming the earlier finding by Chang et al. (2010).

704 Numerical experiments are performed for the August–September 2011 event to ex-
 705 amine the nature of the ionospheric variability associated with the UFKW. When the
 706 UFKW is excluded from the neutral atmosphere, the amplitude of the UFKW spectral
 707 component ($s=-1$, $\tau \sim 3$) in the ionosphere is substantially reduced (Figure 12). This es-

708 establishes that the UFKW causes eastward-propagating \sim 3-day ionospheric variations with
 709 zonal wavenumber 1. The UFKW spectral component in the ionosphere at a fixed lo-
 710 cal time is subject to aliasing from other waves, such as secondary waves due to the non-
 711 linear interaction between the UFKW and migrating tides (Table 2), but the total con-
 712 tribution of those waves to the UFKW spectral component is less than the direct con-
 713 tribution by the UFKW.

714 Numerical results also suggest that it can be difficult for a ground observer to dis-
 715 tinguish between \sim 3-day ionospheric variations associated with the UFKW and those
 716 caused by other sources, as they have comparable amplitudes even during times of en-
 717 hanced UFKW activity (Figure 13). We highlight this issue using ground-based mag-
 718 netometer measurements of the equatorial electrojet during the UFKW event of August–
 719 September 2011. The wavelet spectra of the magnetometer data at different observato-
 720 ries are only in partial agreement, with or without a spectral peak around 3 days. De-
 721 spite that, the combination of the data reveals the predominance of the wave component
 722 with a period of \sim 3 days and zonal wavenumber $s=-1$, corresponding to the UFKW (Fig-
 723 ure 14). This is the first detection of the UFKW in the equatorial electrojet. We em-
 724 phasize that it is important to include measurements from multiple stations when UFKW
 725 signatures in the ionosphere are investigated using ground-based observations.

726 Acknowledgments

727 We thank the NASA Goddard Earth Sciences (GES) Data and Information Ser-
 728 vices Center (DISC) (<https://disc.gsfc.nasa.gov/>) for making the Aura/MLS geopo-
 729 tential height data (DOI: 10.5067/Aura/MLS/DATA2008) available. We also thank the
 730 European Space Agency (ESA) for providing the GOCE TEC data, which can be down-
 731 loaded from http://eo-virtual-archive1.esa.int/GOCE_TEC.html. The GAIA sim-
 732 ulations were performed using the computer system at the Research Institute for Infor-
 733 mation Technology of Kyushu University. The numerical data used in this study are avail-
 734 able from GFZ Data Services (<http://dataservices.gfz-potsdam.de/portal/>). The
 735 GAIA simulations relied on the meteorological data provided from the Japanese 55-year
 736 Reanalysis (JRA-55) project carried out by the Japan Meteorological Agency (JMA).
 737 The magnetic data for Huancayo and Addis Ababa can be downloaded from the INTER-
 738 MAGNET website (www.intermagnet.org). We thank Geophysical Institute of Peru, Ad-
 739 dis Ababa University, and University of Paris for supporting the operation of magnetic

740 field measurements at these observatories. The magnetic data for Tirunelveli can be down-
 741 loaded from the website at the WDC Mumbai (<http://wdciig.res.in>). We thank the
 742 Director, Indian Institute of Geomagnetism (IIG), India for making the Tirunelveli data
 743 available. The Tatuoca magnetic data are accessible from GFZ Data Services ([http://
 744 dataservices.gfz-potsdam.de/panmetaworks/showshort.php?id=escidoc:3504909](http://dataservices.gfz-potsdam.de/panmetaworks/showshort.php?id=escidoc:3504909)).
 745 The magnetic data for Yap Island can be downloaded from the SuperMAG website (supermag.jhuapl.edu). The geomagnetic activity index K_p was provided by the GFZ German
 746 Research Centre for Geosciences (<https://www.gfz-potsdam.de/en/kp-index/>). The
 747 solar activity index $F_{10.7}$ was downloaded from the SPDF OMNIWeb database (<https://omniweb.gsfc.nasa.gov>). Wavelet software provided by C. Torrence and G. Compo is
 748 available at <http://paos.colorado.edu/research/wavelets/>. YY and YM was sup-
 749 ported by the Deutsche Forschungsgemeinschaft (DFG) grant YA-574-3-1 and the Japan
 750 Society for the Promotion of Science (JSPS) grant, respectively, under the joint German-
 751 Japanese project. GBS was supported by Coordenação de Aperfeiçoamento de Pessoal
 752 de Nível Superior – Brasil (CAPES) – Finance Code 1799579 (PhD research grant).
 753

755 References

- 756 Abdu, M. A., Brum, C. G., Batista, P. P., Gurubaran, S., Pancheva, D., Bageston,
 757 J. V., ... Takahashi, H. (2015). Fast and ultrafast Kelvin wave modulations of
 758 the equatorial evening F region vertical drift and spread F development. *Earth,*
 759 *Planets and Space*, 67(1), 1.
- 760 Acker, J. G., & Leptoukh, G. (2007). Online analysis enhances use of nasa earth sci-
 761 ence data. *Eos, Transactions American Geophysical Union*, 88(2), 14–17.
- 762 Alken, P. (2020). Estimating currents and electric fields at low latitudes from satel-
 763 lite magnetic measurements. In *Ionospheric multi-spacecraft analysis tools* (pp.
 764 233–254). Springer.
- 765 Chang, L. C., Palo, S. E., & Liu, H.-L. (2011). Short-term variability in the migrat-
 766 ing diurnal tide caused by interactions with the quasi 2 day wave. *Journal of*
 767 *Geophysical Research: Atmospheres*, 116(D12).
- 768 Chang, L. C., Palo, S. E., Liu, H.-L., Fang, T.-W., & Lin, C. S. (2010). Response of
 769 the thermosphere and ionosphere to an ultra fast Kelvin wave. *Journal of Geo-*
 770 *physical Research: Space Physics*, 115(A8).
- 771 Chen, W.-S., Pan, C., & Das, U. (2018). The mean zonal wind effect on the

- 772 long-term variation of ultra-fast Kelvin waves in the mesosphere and lower
 773 thermosphere and in the upper stratosphere. *Journal of Atmospheric and*
 774 *Solar-Terrestrial Physics*, 179, 459–467.
- 775 Chen, Y.-W., & Miyahara, S. (2012). Analysis of fast and ultrafast Kelvin waves
 776 simulated by the Kyushu-GCM. *Journal of atmospheric and solar-terrestrial*
 777 *physics*, 80, 1–11.
- 778 Cnossen, I., & Richmond, A. D. (2013). Changes in the earth's magnetic field over
 779 the past century: Effects on the ionosphere-thermosphere system and solar
 780 quiet (sq) magnetic variation. *Journal of Geophysical Research: Space Physics*,
 781 118(2), 849–858.
- 782 Davis, R. N., Chen, Y., Miyahara, S., & Mitchell, N. J. (2012). The climatology,
 783 propagation and excitation of ultra-fast Kelvin waves as observed by meteor
 784 radar, Aura MLS, TRMM and in the Kyushu-GCM. *Atmos. Chem. Phys*,
 785 12(4), 1865–1879.
- 786 Egito, F., Buriti, R. A., Medeiros, A. F., & Takahashi, H. (2018). Ultrafast Kelvin
 787 waves in the MLT airglow and wind, and their interaction with the atmo-
 788 spheric tides. *Annales Geophysicae*, 36, 231–241.
- 789 England, S. L., Liu, G., Zhou, Q., Immel, T. J., Kumar, K. K., & Ramkumar, G.
 790 (2012). On the signature of the quasi-3-day wave in the thermosphere during
 791 the january 2010 ursi world day campaign. *Journal of Geophysical Research:*
 792 *Space Physics*, 117(A6).
- 793 Fang, T.-W., Akmaev, R., Fuller-Rowell, T., Wu, F., Maruyama, N., & Millward, G.
 794 (2013). Longitudinal and day-to-day variability in the ionosphere from lower
 795 atmosphere tidal forcing. *Geophysical Research Letters*, 40(11), 2523–2528.
- 796 Finlay, C. C., Olsen, N., Kotsiaros, S., Gillet, N., & Tøffner-Clausen, L. (2016).
 797 Recent geomagnetic secular variation from swarm and ground observatories as
 798 estimated in the chaos-6 geomagnetic field model. *Earth, Planets and Space*,
 799 68(1), 112.
- 800 Forbes, J. M. (2000). Wave coupling between the lower and upper atmosphere:
 801 case study of an ultra-fast Kelvin wave. *Journal of Atmospheric and Solar-*
 802 *Terrestrial Physics*, 62(17-18), 1603–1621.
- 803 Forbes, J. M., Zhang, X., Palo, S. E., Russell, J., Mertens, C. J., & Mlynczak, M.
 804 (2009). Kelvin waves in stratosphere, mesosphere and lower thermosphere tem-

- 805 peratures as observed by TIMED/SABER during 2002–2006. *Earth, planets*
 806 *and space*, 61(4), 447–453.
- 807 Gan, Q., Oberheide, J., & Pedatella, N. M. (2018). Sources, sinks, and propagation
 808 characteristics of the quasi 6-day wave and its impact on the residual mean cir-
 809 culation. *Journal of Geophysical Research: Atmospheres*, 123(17), 9152–9170.
- 810 Gasperini, F., Forbes, J. M., Doornbos, E., & Bruinsma, S. (2015). Wave cou-
 811 pling between the lower and middle thermosphere as viewed from TIMED and
 812 GOCE. *Journal of Geophysical Research: Space Physics*, 120(7), 5788–5804.
- 813 Gasperini, F., Forbes, J. M., Doornbos, E. N., & Bruinsma, S. L. (2018). Kelvin
 814 wave coupling from TIMED and GOCE: Inter/intra-annual variability and
 815 solar activity effects. *Journal of Atmospheric and Solar-Terrestrial Physics*,
 816 171, 176–187.
- 817 Gjerloev, J. (2012). The supermag data processing technique. *Journal of Geophysi-
 818 cal Research: Space Physics*, 117(A9).
- 819 Goncharenko, L., Chau, J., Condor, P., Coster, A., & Benkevitch, L. (2013). Iono-
 820 spheric effects of sudden stratospheric warming during moderate-to-high solar
 821 activity: Case study of january 2013. *Geophysical Research Letters*, 40(19),
 822 4982–4986.
- 823 Gu, S.-Y., Dou, X., Lei, J., Li, T., Luan, X., Wan, W., & Russell III, J. (2014).
 824 Ionospheric response to the ultrafast Kelvin wave in the MLT region. *Journal*
 825 *of Geophysical Research: Space Physics*, 119(2), 1369–1380.
- 826 Gu, S.-Y., Dou, X.-K., Yang, C.-Y., Jia, M., Huang, K.-M., Huang, C.-M., & Zhang,
 827 S.-D. (2018). Climatology and anomaly of the quasi-two-day wave behaviors
 828 during 2003–2018 austral summer periods. *Journal of Geophysical Research:
 829 Space Physics*.
- 830 Gu, S.-Y., Ruan, H., Yang, C.-Y., Gan, Q., Dou, X., & Wang, N. (2018). The
 831 morphology of the 6-day wave in both the neutral atmosphere and F region
 832 ionosphere under solar minimum conditions. *Journal of Geophysical Research:
 833 Space Physics*, 123(5), 4232–4240.
- 834 Gurubaran, S., Dhanya, R., Sathiskumar, S., & Patil, P. (2011). A case study of
 835 tidal and planetary wave coupling in the equatorial atmosphere-ionosphere
 836 system over india: preliminary results. In *Aeronomy of the earth's atmosphere
 837 and ionosphere* (pp. 177–187). Springer.

- 838 Hayashi, Y. (1971). A generalized method of resolving disturbances into progres-
 839 sive and retrogressive waves by space fourier and time cross-spectral analyses.
 840 *Journal of the Meteorological Society of Japan. Ser. II*, 49(2), 125–128.
- 841 Hirota, I. (1978). Equatorial waves in the upper stratosphere and mesosphere in
 842 relation to the semiannual oscillation of the zonal wind. *Journal of the Atmo-*
 843 *spheric Sciences*, 35(4), 714–722.
- 844 Hirota, I. (1979). Kelvin waves in the equatorial middle atmosphere observed by the
 845 Nimbus 5. SCR. *Journal of the Atmospheric Sciences*, 36(2), 217–222.
- 846 Holton, J. R., & Lindzen, R. S. (1968). A note on “kelvin” waves in the atmosphere.
 847 *Mon. Wea. Rev.*, 96(6), 385–386.
- 848 Jarvis, M. (2006). Planetary wave trends in the lower thermosphere—evidence for
 849 22-year solar modulation of the quasi 5-day wave. *Journal of atmospheric and*
 850 *solar-terrestrial physics*, 68(17), 1902–1912.
- 851 Jin, H., Miyoshi, Y., Fujiwara, H., & Shinagawa, H. (2008). Electrodynamics of
 852 the formation of ionospheric wave number 4 longitudinal structure. *Journal of*
 853 *Geophysical Research: Space Physics*, 113(A9).
- 854 Jin, H., Miyoshi, Y., Fujiwara, H., Shinagawa, H., Terada, K., Terada, N., ... Saito,
 855 A. (2011). Vertical connection from the tropospheric activities to the iono-
 856 spheric longitudinal structure simulated by a new earth’s whole atmosphere-
 857 ionosphere coupled model. *Journal of Geophysical Research: Space Physics*,
 858 116(A1).
- 859 Jin, H., Miyoshi, Y., Pancheva, D., Mukhtarov, P., Fujiwara, H., & Shinagawa, H.
 860 (2012). Response of migrating tides to the stratospheric sudden warming
 861 in 2009 and their effects on the ionosphere studied by a whole atmosphere-
 862 ionosphere model GAIA with COSMIC and TIMED/SABER observations.
 863 *Journal of Geophysical Research: Space Physics*, 117(A10).
- 864 Jonah, O. F., de Paula, E., Kherani, E., Dutra, S., & Paes, R. (2014). Atmospheric
 865 and ionospheric response to sudden stratospheric warming of january 2013.
 866 *Journal of Geophysical Research: Space Physics*, 119(6), 4973–4980.
- 867 Kervalishvili, G., Xiong, C., Stolle, C., Rauberg, J., & van den IJssse, J. (2018).
 868 *Computation of tec and rate of tec index (roti) from goce gps* (Tech. Rep. No.
 869 GO-TN-HPF-GS-0337). Paris, Île-de-France, France: ESA.
- 870 Kobayashi, S., Ota, Y., Harada, Y., Ebita, A., Moriya, M., Onoda, H., ... others

- 871 (2015). The JRA-55 reanalysis: General specifications and basic characteristics. *Journal of the Meteorological Society of Japan. Ser. II*, 93(1), 5–48.
- 872 Lieberman, R. S., & Riggan, D. (1997). High resolution Doppler imager observations
873 of Kelvin waves in the equatorial mesosphere and lower thermosphere. *Journal
874 of Geophysical Research: Atmospheres*, 102(D22), 26117–26130.
- 875 Liu, G., England, S. L., Immel, T. J., Kumar, K. K., Ramkumar, G., & Gon-
876 charenko, L. P. (2012). Signatures of the 3-day wave in the low-latitude
877 and midlatitude ionosphere during the january 2010 ursi world day campaign.
878 *Journal of Geophysical Research: Space Physics*, 117(A6).
- 879 Liu, G., England, S. L., & Janches, D. (2019). Quasi two-, three-, and six-
880 day planetary-scale wave oscillations in the upper atmosphere observed by
881 TIMED/SABER over ∼17 years during 2002–2018. *Journal of Geophysical
882 Research: Space Physics*, 124(11), 9462–9474.
- 883 Liu, H.-L. (2016). Variability and predictability of the space environment as related
884 to lower atmosphere forcing. *Space Weather*, 14(9), 634–658.
- 885 Livesey, N., Read, W., Wagner, P., Froidevaux, L., Lambert, A., Manney, G.,
886 ... others (2017). Earth Observing System (EOS), Aura Microwave
887 Limb Sounder (MLS), Version 4.2 x Level 2 data quality and descrip-
888 tion document, Version 4.2 x-3.0, D-33509. *Jet Propulsion Laboratory,
889 California Institute of Technology, Pasadena, California, available at:
890 https://mls.jpl.nasa.gov/data/datadocs.php, last access, 7.*
- 891 Love, J. J., & Chulliat, A. (2013). An international network of magnetic observato-
892 ries. *Eos, Transactions American Geophysical Union*, 94(42), 373–374.
- 893 Lühr, H., Xiong, C., Olsen, N., & Le, G. (2017). Near-earth magnetic field effects
894 of large-scale magnetospheric currents. *Space Science Reviews*, 206(1-4), 521–
895 545.
- 896 Matsuno, T. (1966). Quasi-geostrophic motions in the equatorial area. *Journal of
897 the Meteorological Society of Japan. Ser. II*, 44(1), 25–43.
- 898 Matzka, J., Siddiqui, T. A., Lilienkamp, H., Stolle, C., & Veliz, O. (2017). Quan-
899 tifying solar flux and geomagnetic main field influence on the equatorial iono-
900 spheric current system at the geomagnetic observatory huancayo. *Journal of
901 Atmospheric and Solar-Terrestrial Physics*, 163, 120–125.
- 902 Maute, A., Hagan, M., Yudin, V., Liu, H.-L., & Yizengaw, E. (2015). Causes of

- 904 the longitudinal differences in the equatorial vertical $E \times B$ drift during the
 905 2013 SSW period as simulated by the TIME-GCM. *Journal of Geophysical*
 906 *Research: Space Physics*, 120(6), 5117–5136.
- 907 Miyoshi, Y., & Fujiwara, H. (2003). Day-to-day variations of migrating diurnal tide
 908 simulated by a GCM from the ground surface to the exobase. *Geophysical re-*
 909 *search letters*, 30(15).
- 910 Miyoshi, Y., & Fujiwara, H. (2006). Excitation mechanism of intraseasonal oscil-
 911 lation in the equatorial mesosphere and lower thermosphere. *Journal of Geo-*
 912 *physical Research: Atmospheres*, 111(D14).
- 913 Miyoshi, Y., Fujiwara, H., Jin, H., Shinagawa, H., Liu, H., & Terada, K. (2011).
 914 Model study on the formation of the equatorial mass density anomaly in the
 915 thermosphere. *Journal of Geophysical Research: Space Physics*, 116(A5).
- 916 Miyoshi, Y., Pancheva, D., Mukhtarov, P., Jin, H., Fujiwara, H., & Shinagawa, H.
 917 (2017). Excitation mechanism of non-migrating tides. *Journal of Atmospheric*
 918 *and Solar-Terrestrial Physics*, 156, 24–36.
- 919 Morschhauser, A., Soares, G. B., Haseloff, J., Bronkalla, O., Protásio, J., Pinheiro,
 920 K., & Matzka, J. (2017). The magnetic observatory on Tatuoca, Belém, Brazil:
 921 history and recent developments. *Geoscientific Instrumentation, Methods and*
 922 *Data Systems*, 6(2), 367.
- 923 Noja, M., Stolle, C., Park, J., & Lühr, H. (2013). Long-term analysis of ionospheric
 924 polar patches based on champ tec data. *Radio Science*, 48(3), 289–301.
- 925 Nystrom, V., Gasperini, F., Forbes, J. M., & Hagan, M. E. (2018). Exploring wave-
 926 wave interactions in a general circulation model. *Journal of Geophysical Re-*
 927 *search: Space Physics*, 123(1), 827–847.
- 928 Onogi, K., Tsutsui, J., Koide, H., Sakamoto, M., Kobayashi, S., Hatsushika, H., ...
 929 others (2007). The JRA-25 reanalysis. *Journal of the Meteorological Society of*
 930 *Japan. Ser. II*, 85(3), 369–432.
- 931 Onohara, A., Batista, I., & Takahashi, H. (2013). The ultra-fast Kelvin waves in
 932 the equatorial ionosphere: observations and modeling. *Annales Geophysicae*
 933 (09927689), 31(2).
- 934 Pancheva, D., Mitchell, N., & Younger, P. (2004). Meteor radar observations of
 935 atmospheric waves in the equatorial mesosphere/lower thermosphere over
 936 ascension island. In (Vol. 22, pp. 387–404).

- 937 Pancheva, D., Mukhtarov, P., Mitchell, N., Fritts, D., Riggin, D., Takahashi, H.,
 938 ... Ramkumar, G. (2008). Planetary wave coupling (5–6-day waves) in the
 939 low-latitude atmosphere–ionosphere system. *Journal of Atmospheric and*
 940 *Solar-Terrestrial Physics*, 70(1), 101–122.
- 941 Pancheva, D., Mukhtarov, P., Shepherd, M., Mitchell, N., Fritts, D., Riggin, D.,
 942 ... others (2006). Two-day wave coupling of the low-latitude atmosphere–
 943 ionosphere system. *Journal of Geophysical Research: Space Physics*, 111(A7).
- 944 Pancheva, D., Mukhtarov, P., & Siskind, D. E. (2018). Climatology of the quasi-
 945 2-day waves observed in the MLS/Aura measurements (2005–2014). *Journal of*
 946 *Atmospheric and Solar-Terrestrial Physics*, 171, 210–224.
- 947 Pedatella, N., Liu, H.-L., & Hagan, M. (2012). Day-to-day migrating and nonmigrat-
 948 ing tidal variability due to the six-day planetary wave. *Journal of Geophysical*
 949 *Research: Space Physics*, 117(A6).
- 950 Phanikumar, D., Kumar, K. N., & Kumar, S. (2014). Signatures of ultra fast Kelvin
 951 waves in low latitude ionospheric TEC during January 2009 stratospheric
 952 warming event. *Journal of Atmospheric and Solar-Terrestrial Physics*, 117,
 953 48–53.
- 954 Ramkumar, T., Gurubaran, S., & Rajaram, R. (2009). Mesospheric planetary wave
 955 signatures in the equatorial electrojet. *Journal of Geophysical Research: Space*
 956 *Physics*, 114(A3).
- 957 Riggin, D. M., Fritts, D. C., Tsuda, T., Nakamura, T., & Vincent, R. A. (1997).
 958 Radar observations of a 3-day Kelvin wave in the equatorial mesosphere. *Jour-*
 959 *nal of Geophysical Research: Atmospheres*, 102(D22), 26141–26157.
- 960 Salby, M. L., Hartmann, D. L., Bailey, P. L., & Gille, J. C. (1984). Evidence for
 961 equatorial Kelvin modes in Nimbus-7 LIMS. *Journal of the atmospheric sci-*
 962 *ences*, 41(2), 220–235.
- 963 Sassi, F., Liu, H.-L., Ma, J., & Garcia, R. R. (2013). The lower thermosphere during
 964 the northern hemisphere winter of 2009: A modeling study using high-altitude
 965 data assimilation products in WACCM-X. *Journal of Geophysical Research:*
 966 *Atmospheres*, 118(16), 8954–8968.
- 967 Schwartz, M., Lambert, A., Manney, G., Read, W., Livesey, N., Froidevaux, L., ...
 968 others (2008). Validation of the Aura Microwave Limb Sounder tempera-
 969 ture and geopotential height measurements. *Journal of Geophysical Research:*

- 970 *Atmospheres*, 113(D15).
- 971 Shinagawa, H. (2011). Ionosphere simulation. *Journal of NICT*, 56(1-4), 199–207.
- 972 Siddiqui, T. A., Yamazaki, Y., Stolle, C., Lühr, H., Matzka, J., Maute, A., & Pe-
973 datella, N. (2018). Dependence of lunar tide of the equatorial electrojet on
974 the wintertime polar vortex, solar flux, and qbo. *Geophysical Research Letters*,
975 45(9), 3801–3810.
- 976 Soares, G., Matzka, J., & Pinheiro, K. (2018). Preliminary minute means geomag-
977 netic observatory tatuoca (TTB), 2008 to 2017. Retrieved from <http://doi.org/10.5880/GFZ.2.3.2018.005> doi: 10.5880/GFZ.2.3.2018.005
- 979 Soares, G., Yamazaki, Y., Matzka, J., Pinheiro, K., Morschhauser, A., Stolle, C., &
980 Alken, P. (2018). Equatorial counter electrojet longitudinal and seasonal vari-
981 ability in the american sector. *Journal of Geophysical Research: Space Physics*,
982 123(11), 9906–9920.
- 983 Sridharan, S., Gurubaran, S., & Rajaram, R. (2002). Radar observations of the
984 3.5-day ultra-fast Kelvin wave in the low-latitude mesopause region. *Journal of
985 Atmospheric and Solar-Terrestrial Physics*, 64(8-11), 1241–1250.
- 986 Stolle, C., Manoj, C., Lühr, H., Maus, S., & Alken, P. (2008). Estimating the day-
987 time equatorial ionization anomaly strength from electric field proxies. *Journal
988 of Geophysical Research: Space Physics*, 113(A9).
- 989 Takahashi, H., Wrassse, C., Fechine, J., Pancheva, D., Abdu, M., Batista, I., ... oth-
990 ers (2007). Signatures of ultra fast Kelvin waves in the equatorial middle
991 atmosphere and ionosphere. *Geophysical research letters*, 34(11).
- 992 Takahashi, H., Wrassse, C., Pancheva, D., Abdu, M., Batista, I., Lima, L., ... Sh-
993 iokawa, K. (2006). Signatures of 3–6 day planetary waves in the equatorial
994 mesosphere and ionosphere. *Annales geophysicae*, 24, 3343–3350.
- 995 Takeda, M. (1996). Effects of the strength of the geomagnetic main field strength on
996 the dynamo action in the ionosphere. *Journal of Geophysical Research: Space
997 Physics*, 101(A4), 7875–7880.
- 998 Tapping, K. (2013). The 10.7 cm solar radio flux ($F_{10.7}$). *Space Weather*, 11(7),
999 394–406.
- 1000 Teitelbaum, H., & Vial, F. (1991). On tidal variability induced by nonlinear inter-
1001 action with planetary waves. *Journal of Geophysical Research: Space Physics*,
1002 96(A8), 14169–14178.

- 1003 Torrence, C., & Compo, G. P. (1998). A practical guide to wavelet analysis. *Bulletin*
1004 *of the American Meteorological society*, 79(1), 61–78.
- 1005 Triplet, C. C., Immel, T. J., Wu, Y.-J., & Cullens, C. (2019). Variations in the
1006 ionosphere-thermosphere system from tides, ultra-fast Kelvin waves, and their
1007 interactions. *Advances in Space Research*, 64(10), 1841–1853.
- 1008 Vincent, R. (1993). Long-period motions in the equatorial mesosphere. *Journal of*
1009 *atmospheric and terrestrial physics*, 55(7), 1067–1080.
- 1010 Wallace, J. M., & Kousky, V. (1968). Observational evidence of Kelvin waves in the
1011 tropical stratosphere. *Journal of the Atmospheric Sciences*, 25(5), 900–907.
- 1012 Waters, J. W., Froidevaux, L., Harwood, R. S., Jarnot, R. F., Pickett, H. M., Read,
1013 W. G., ... others (2006). The earth observing system microwave limb sounder
1014 (EOS MLS) on the Aura satellite. *IEEE Transactions on Geoscience and*
1015 *Remote Sensing*, 44(5), 1075–1092.
- 1016 Xiong, C., Lühr, H., & Fejer, B. G. (2016). The response of equatorial electrojet,
1017 vertical plasma drift, and thermospheric zonal wind to enhanced solar wind
1018 input. *Journal of Geophysical Research: Space Physics*, 121(6), 5653–5663.
- 1019 Yamazaki, Y., & Kosch, M. J. (2015). The equatorial electrojet during geomag-
1020 netic storms and substorms. *Journal of Geophysical Research: Space Physics*,
1021 120(3), 2276–2287.
- 1022 Yamazaki, Y., & Matthias, V. (2019). Large-amplitude quasi-10-day waves in
1023 the middle atmosphere during final warmings. *Journal of Geophysical Re-*
1024 *search: Atmospheres*, 124(17-18), 9874–9892. Retrieved from <https://agupubs.onlinelibrary.wiley.com/doi/abs/10.1029/2019JD030634> doi:
1025 10.1029/2019JD030634
- 1027 Yamazaki, Y., & Maute, A. (2017). Sq and EEJ—A review on the daily variation
1028 of the geomagnetic field caused by ionospheric dynamo currents. *Space Science*
1029 *Reviews*, 206(1-4), 299–405.
- 1030 Yamazaki, Y., Richmond, A., Maute, A., Liu, H.-L., Pedatella, N., & Sassi, F.
1031 (2014). On the day-to-day variation of the equatorial electrojet during quiet
1032 periods. *Journal of Geophysical Research: Space Physics*, 119(8), 6966–6980.
- 1033 Yamazaki, Y., Stolle, C., Matzka, J., Liu, H., & Tao, C. (2018). Interannual variabil-
1034 ity of the daytime equatorial ionospheric electric field. *Journal of Geophysical*
1035 *Research: Space Physics*, 123(5), 4241–4256.

- 1036 Yigit, E., & Medvedev, A. S. (2015). Internal wave coupling processes in earth's at-
1037 mosphere. *Advances in Space Research*, 55(4), 983–1003.
- 1038 Yoshida, S., Tsuda, T., Shimizu, A., & Nakamura, T. (1999). Seasonal variations
1039 of 3.0–3.8-day ultra-fast Kelvin waves observed with a meteor wind radar and
1040 radiosonde in indonesia. *Earth, planets and space*, 51(7-8), 675–684.
- 1041 Yue, J., Wang, W., Richmond, A. D., Liu, H.-L., & Chang, L. C. (2013). Wavenum-
1042 ber broadening of the quasi 2 day planetary wave in the ionosphere. *Journal of*
1043 *Geophysical Research: Space Physics*, 118(6), 3515–3526.
- 1044 Yumoto, K., & the MAGDAS Group. (2006). Magdas project and its application for
1045 space weather. In N. Gopalswamy & A. Bhattacharyya (Eds.), *Solar influence*
1046 *on the heliosphere and earth's environment: Recent progress and prospects* (pp.
1047 309–405). Mumbai, India: Quest Publ.

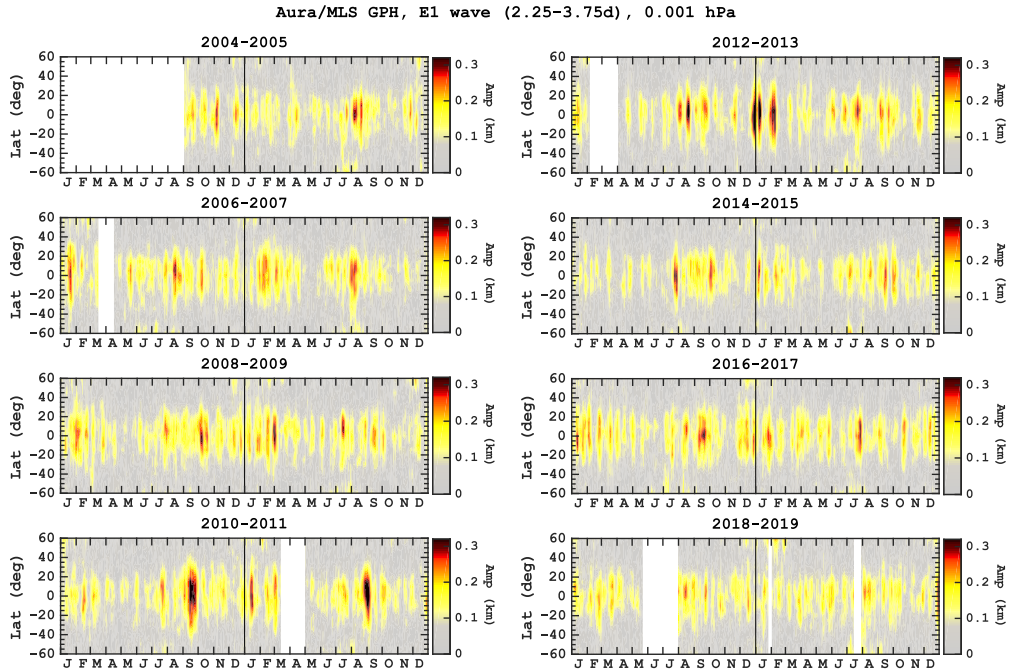


Figure 1. Amplitude of the ultra-fast Kelvin wave (UFWK) as derived from the geopotential height (GPH) measurements at 0.001 hPa (~ 97 km altitude) by the Aura Microwave Limb Sounder during 2004–2019. The UFWK amplitude is defined as the largest amplitude of the eastward-propagating waves with zonal wavenumber 1 within periods of 2.25–3.75 days.

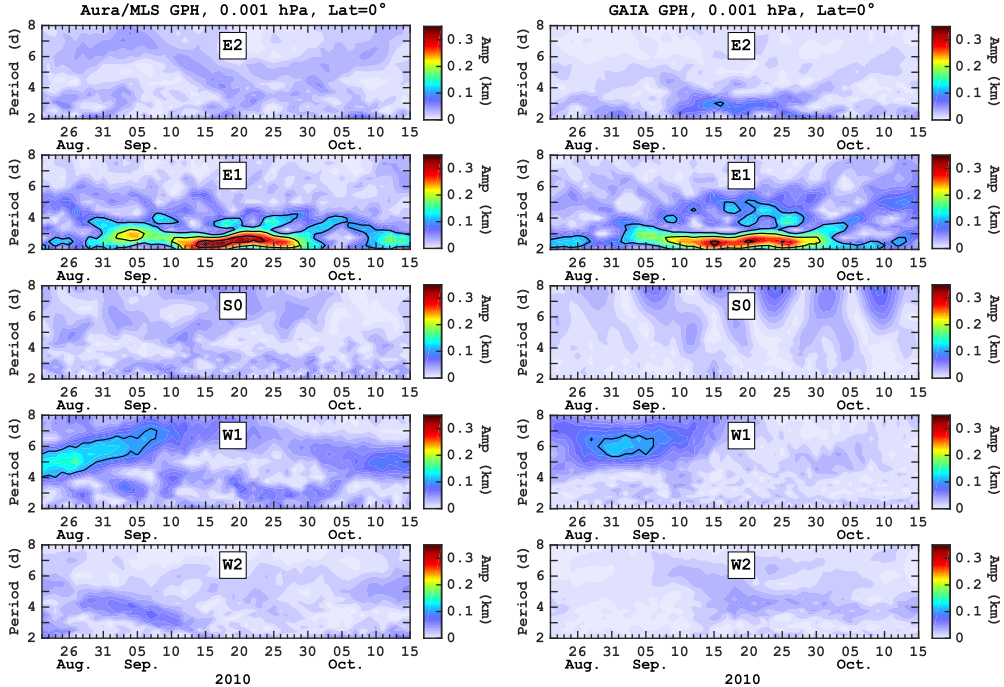


Figure 2. Time versus period diagrams of the wave spectrum derived from the geopotential height (GPH) at 0.001 hPa (~ 97 km altitude) over the equator for zonal wavenumber $s = -2$ (E2), $s = -1$ (E1), $s = 0$ (S0), $s = +1$ (W1), and $s = +2$ (W2) during the ultra-fast Kelvin wave (UFWK) event of September 2010. The left panels are from the Aura Microwave Limb Sounder measurements while the right panels are from the GAIA model.

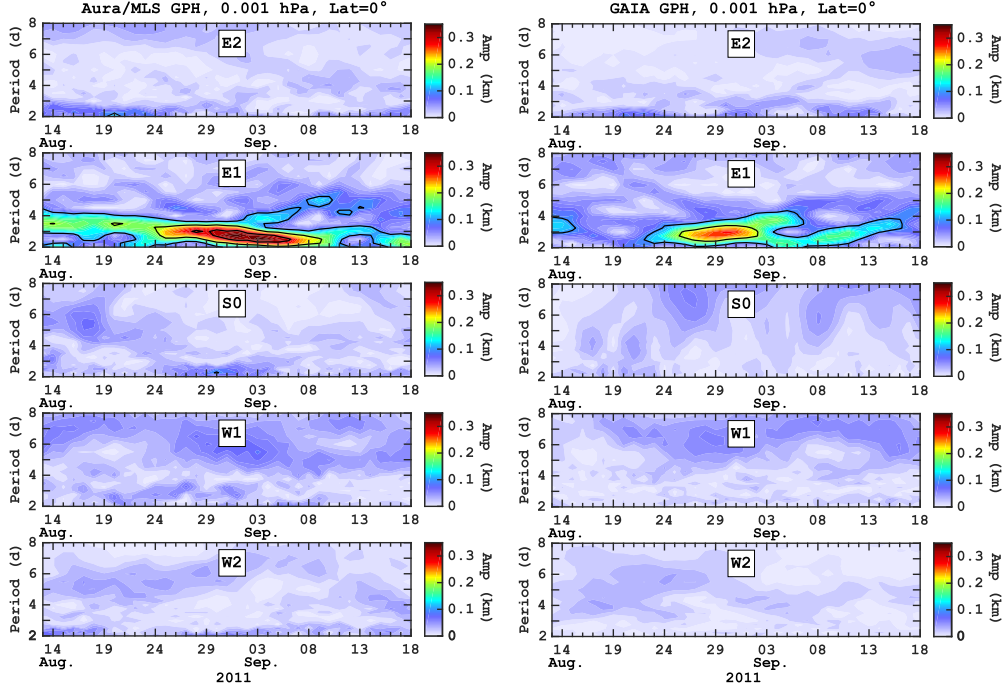


Figure 3. Same as Figure 2 except for the ultra-fast Kelvin wave (UFWK) event of August–September 2011.

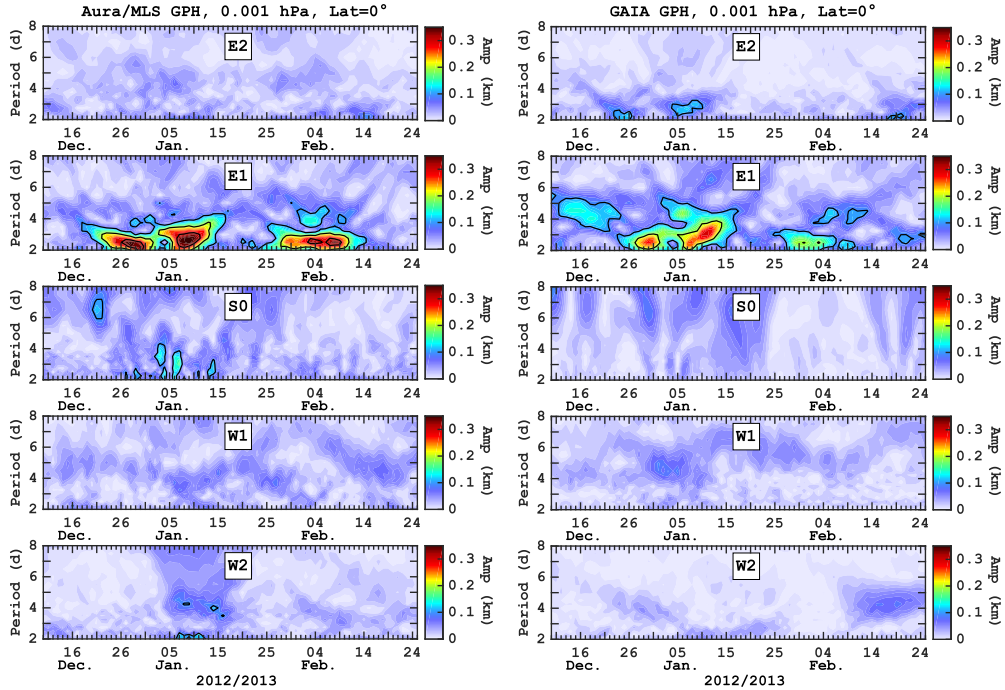


Figure 4. Same as Figure 2 except for the ultra-fast Kelvin wave (UFWK) event of December 2012–January 2013.

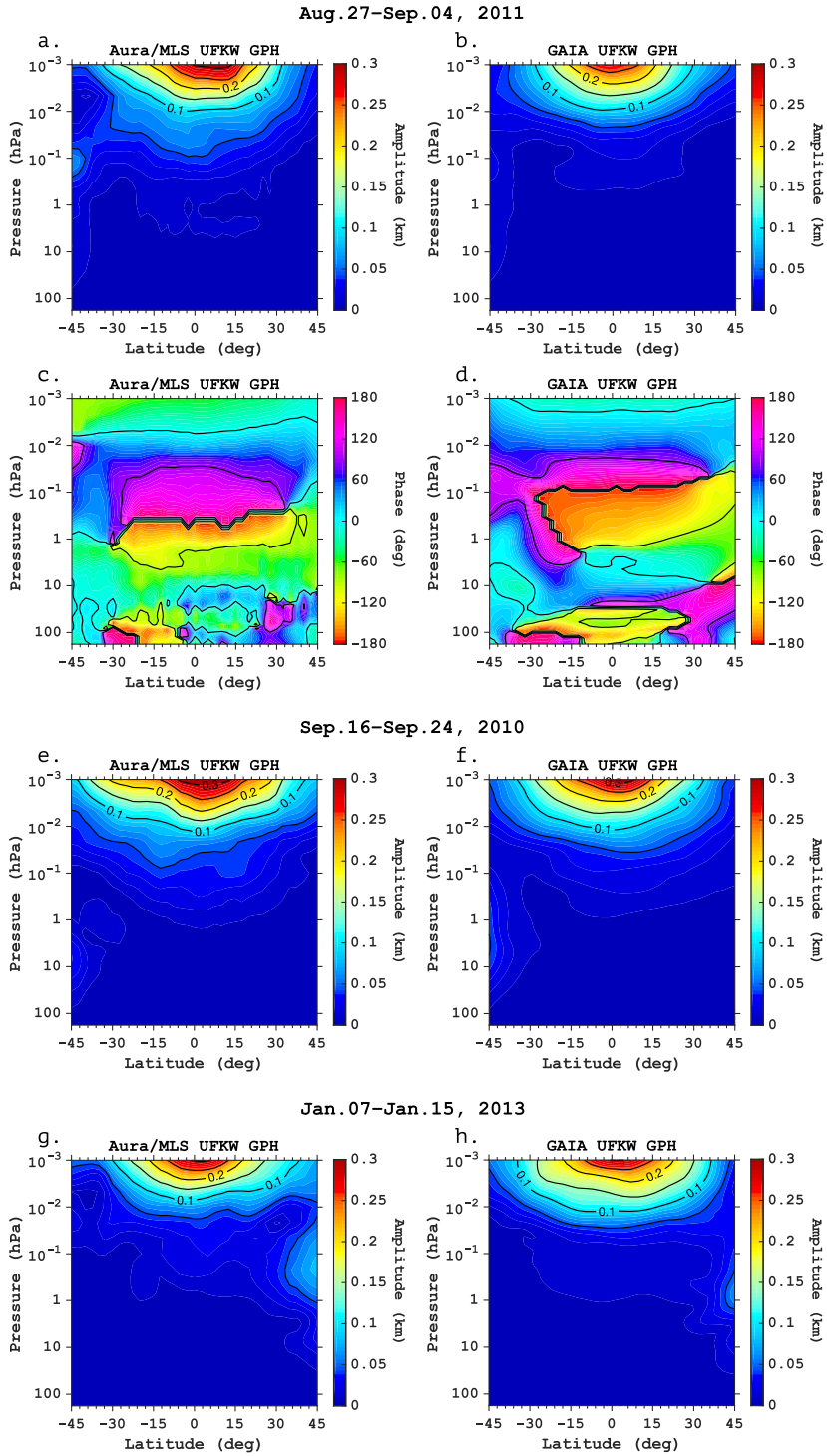


Figure 5. Latitude versus height structures of the ultra-fast Kelvin wave (UFKW) in the geopotential height (GPH) during the August–September 2011 event (a–d), the September 2010 event (e, f), and the December 2012–January 2013 event (g, h). The left panels are from the Aura Microwave Limb Sounder (MLS) measurements while the right panels are from the GAIA model. The panels (a, b, and e–h) show the amplitude while the panels (c, d) show the phase. The vertical range covers the pressure levels from 261 to 0.001 hPa, which corresponds to approximately 9–97 km altitude.

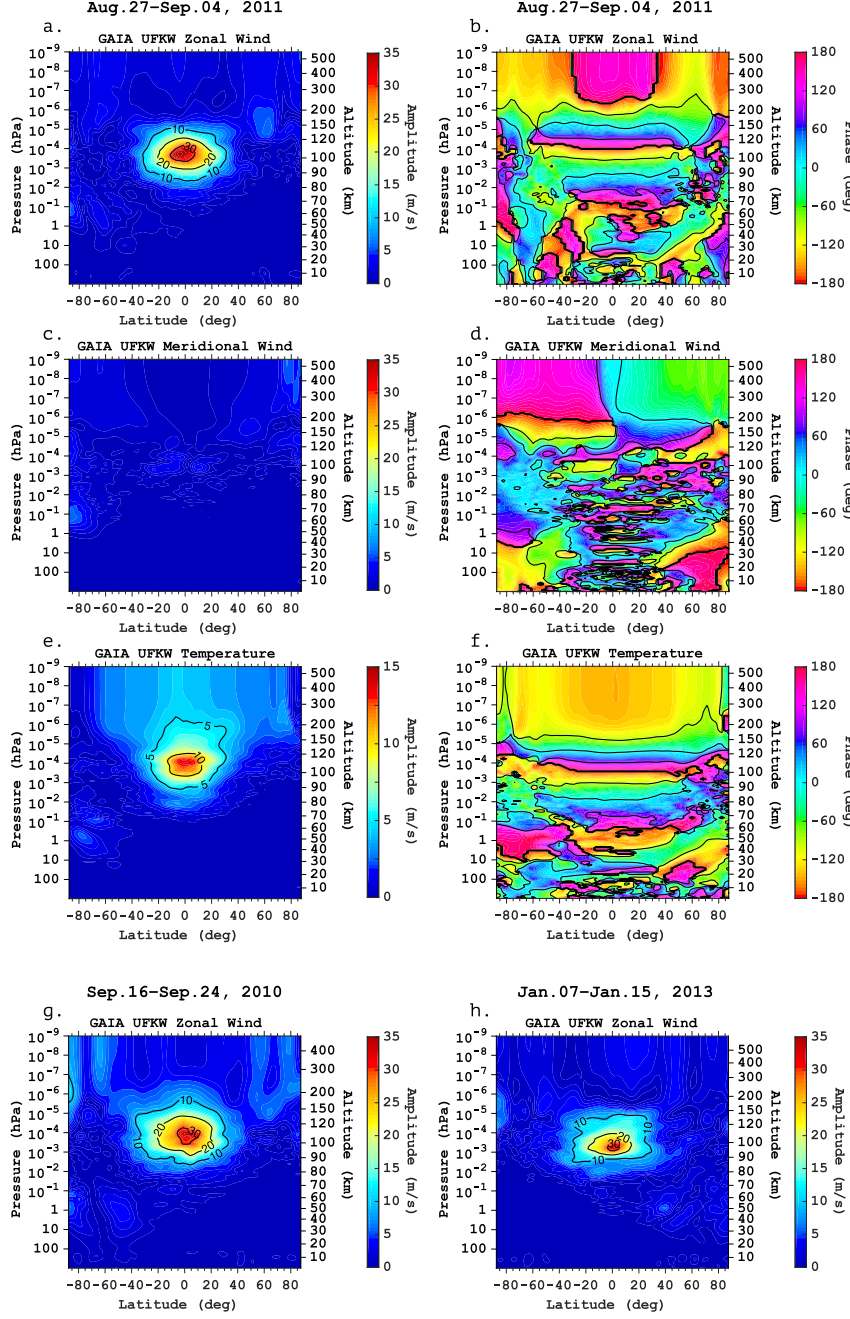


Figure 6. Latitude versus height structures of the ultra-fast Kelvin wave (UFWK) in the zonal wind (a, b, g, h), meridional wind (c, d), and temperature (e, f) derived from the GAIA model. The panels (a–f) are for the UFWK event of August–September 2011 event, showing the amplitude on the left and the phase on the right. The panels (g) and (h) show the UFWK amplitude in the zonal wind during the September 2010 event and the December 2012–January 2013 event, respectively. The UFWK is defined as the eastward-propagating wave with a period of 3.0 days and zonal wavenumber 1 for the August–September 2011 event and the December 2012–January 2013 event, while for the September 2010 event, the wave with a period of 2.5 days is considered.

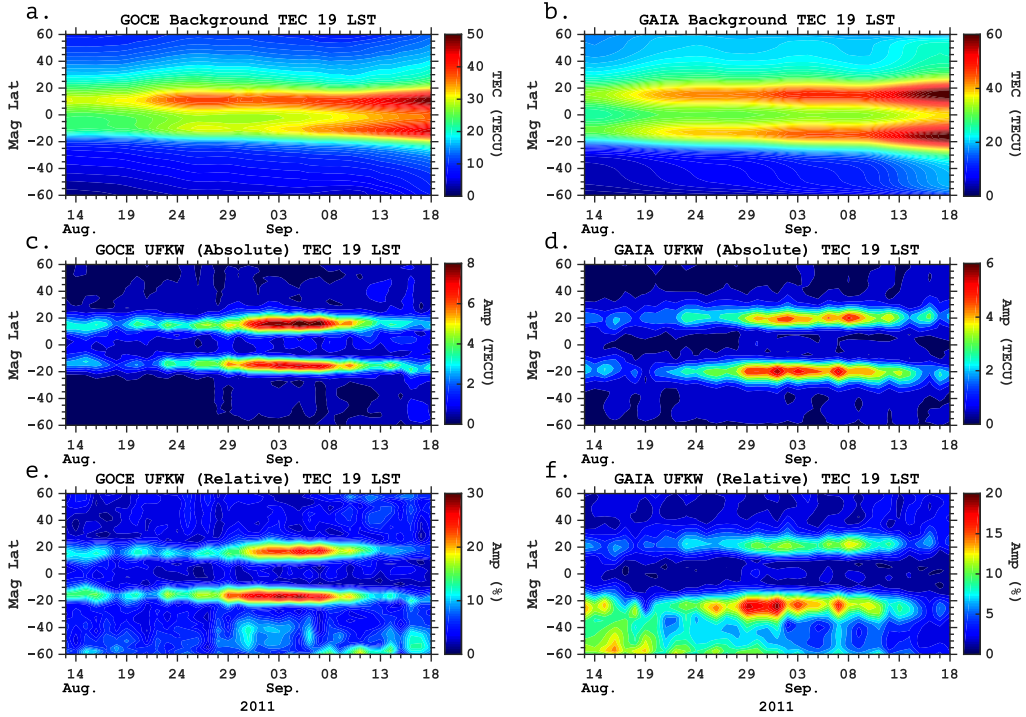


Figure 7. Comparison of the total electron content (TEC) at 7 p.m. local solar time derived from the GOCE measurements (a, c, e) and GAIA model (b, d, f). The panels (a, b) show the background total electron content (TEC) as defined here as the temporal and zonal mean calculated at each latitude using a 9-day moving window. The panels (c, d) show the amplitude of the ultra-fast Kelvin wave (UFKW) spectral component in TEC calculated at each latitude using the 9-day moving window. The UKFW spectral component is defined as the largest amplitude of the eastward-propagating waves with zonal wavenumber 1 within periods 2.25–3.75 days. The panels (e, f) show the relative amplitude of the UKFW spectral component in TEC with respect to the corresponding background TEC value. Note that color scales are different for different panels.

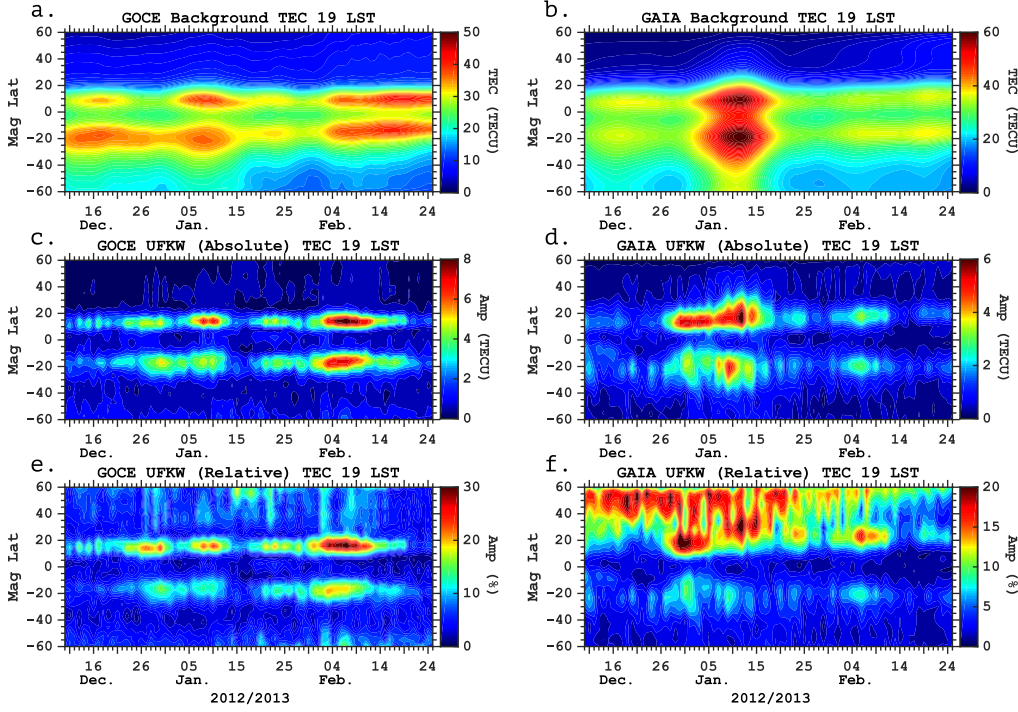


Figure 8. Same as Figure 7 except for the December 2012–January 2013 event.

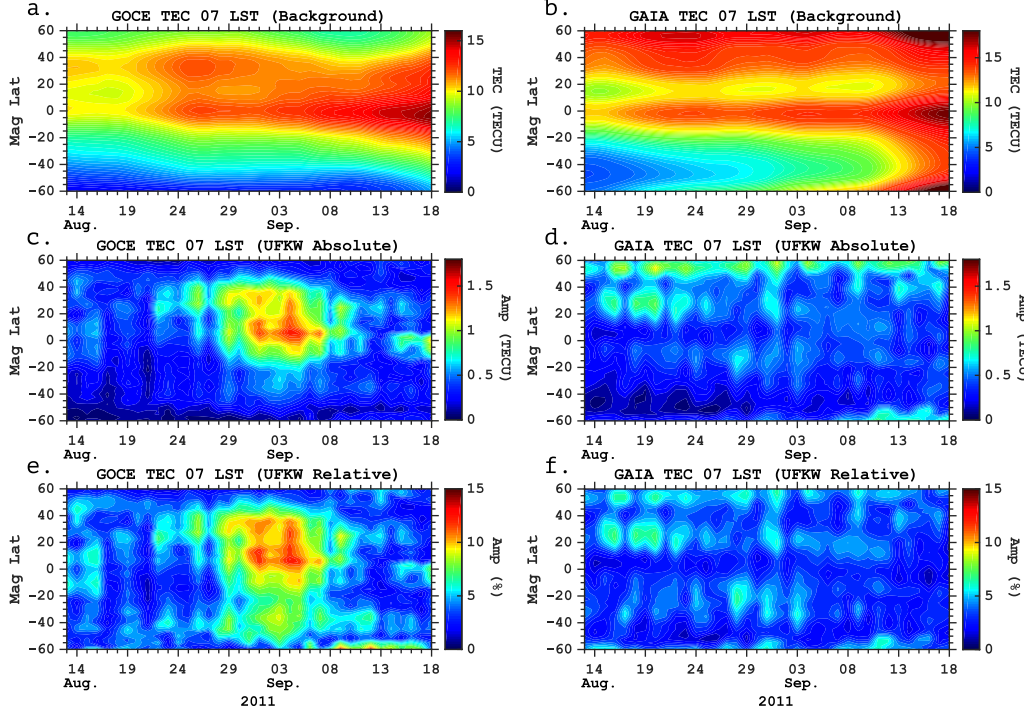


Figure 9. Same as Figure 7 except for 7 a.m. local solar time.

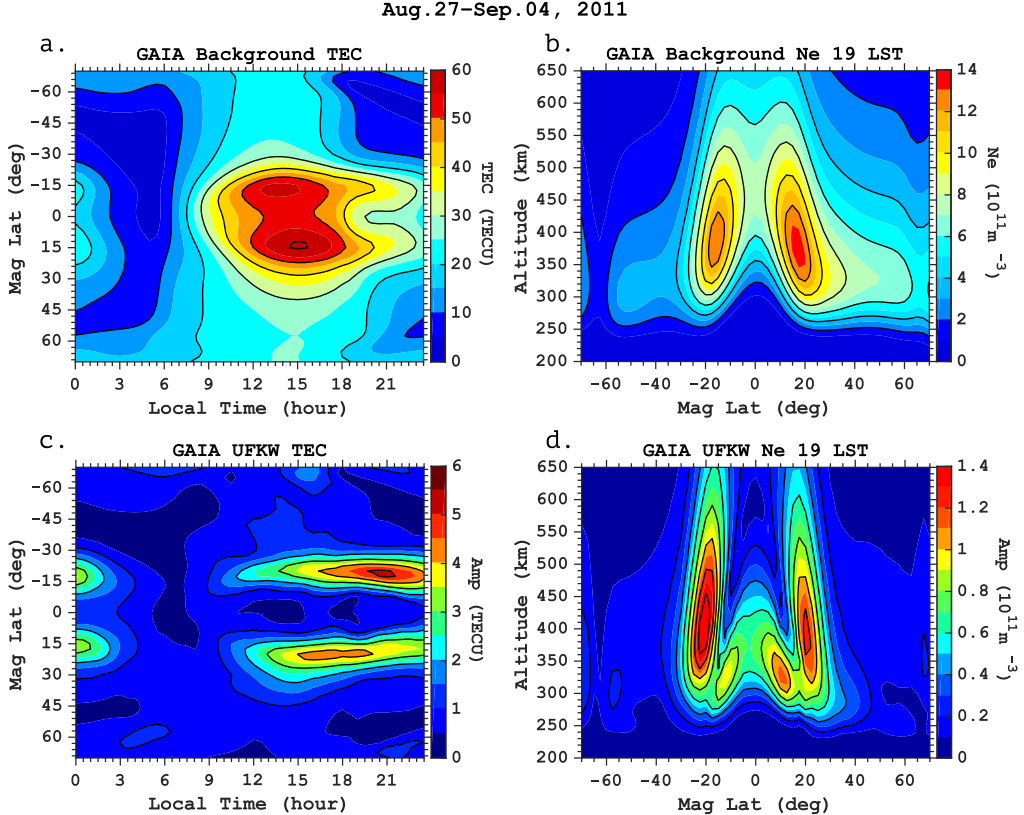


Figure 10. Spatial structure of the amplitude of the ultra-fast Kelvin wave (UFWK) spectral component in total electron content (TEC) and electron density (N_e) during the August–September 2011 event. (a) Local-time and magnetic-latitude dependence of the background TEC. (b) Magnetic-latitude and height dependence of the background electron density at 7 p.m. local solar time. (c) Same as (a) except for the the amplitude of the UFWK spectral component in TEC. (d) Same as (b) except for the amplitude of the UFWK spectral component in the electron density.

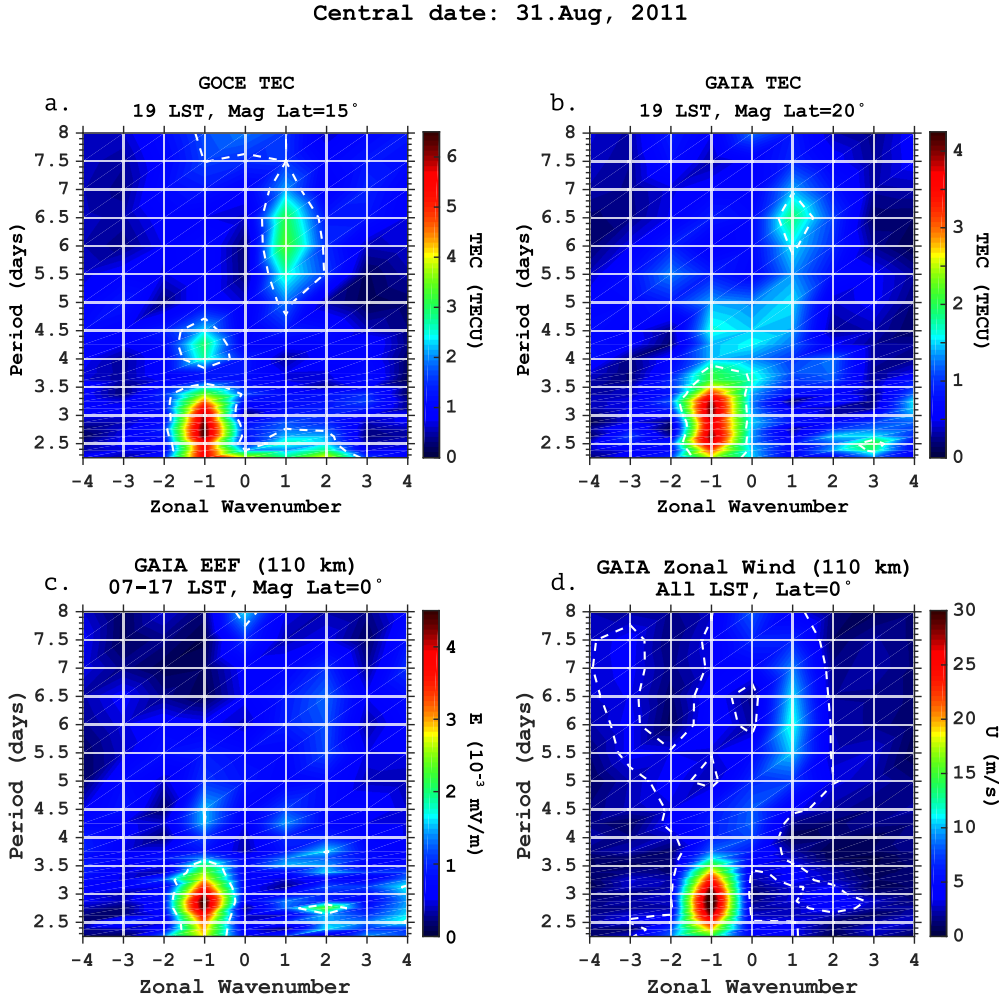


Figure 11. Wavenumber versus period spectra during the ultra-fast Kelvin wave event of August–September 2011. The panel (a) is for the total electron content (TEC) derived from the GOCE measurements at 7 p.m. local solar time and 15° magnetic latitude. The panel (b) shows the same as (a) except for TEC at 20° magnetic latitude from the GAIA model. The panel (c) is also from GAIA but for the equatorial zonal electric field (EEF) between 7 a.m. and 5 p.m. local solar time at 110 km altitude. The panel (d) is for the zonal wind at the equator at 110 km altitude. The white dashed lines correspond to the 95% confidence level.

Central date: 31.Aug, 2011

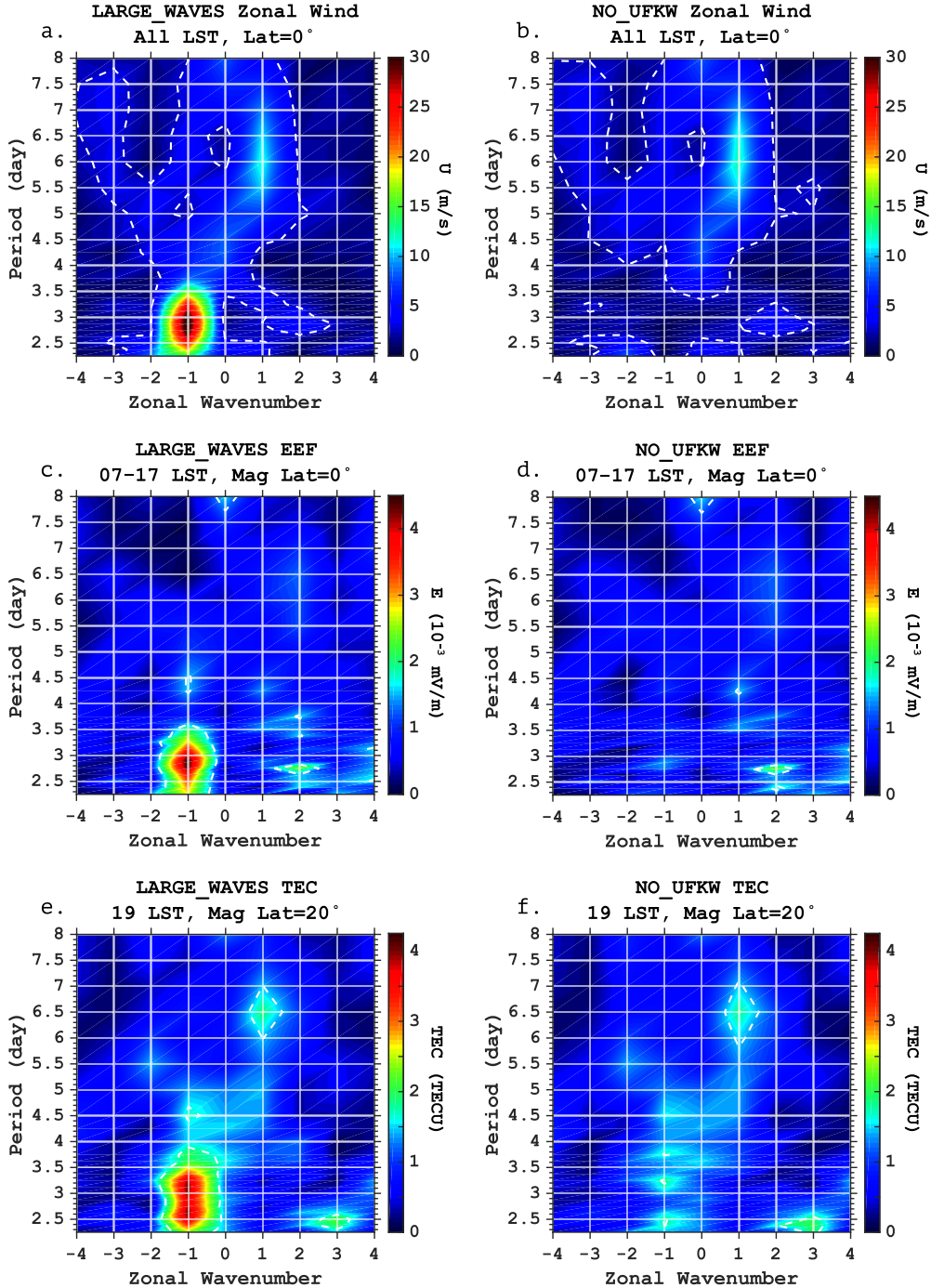


Figure 12. Wavenumber versus period spectra during the ultra-fast Kelvin wave event of August–September 2011. The panels (a) and (b) are the same as Figure 11d except for LARGE_WAVES and NO_UFKW simulation cases, respectively. The panels (c) and (d) are the same as Figure 11c except for LARGE_WAVES and NO_UFKW simulation cases, respectively. The panels (e) and (f) are the same as Figure 11b except for LARGE_WAVES and NO_UFKW simulation cases, respectively.

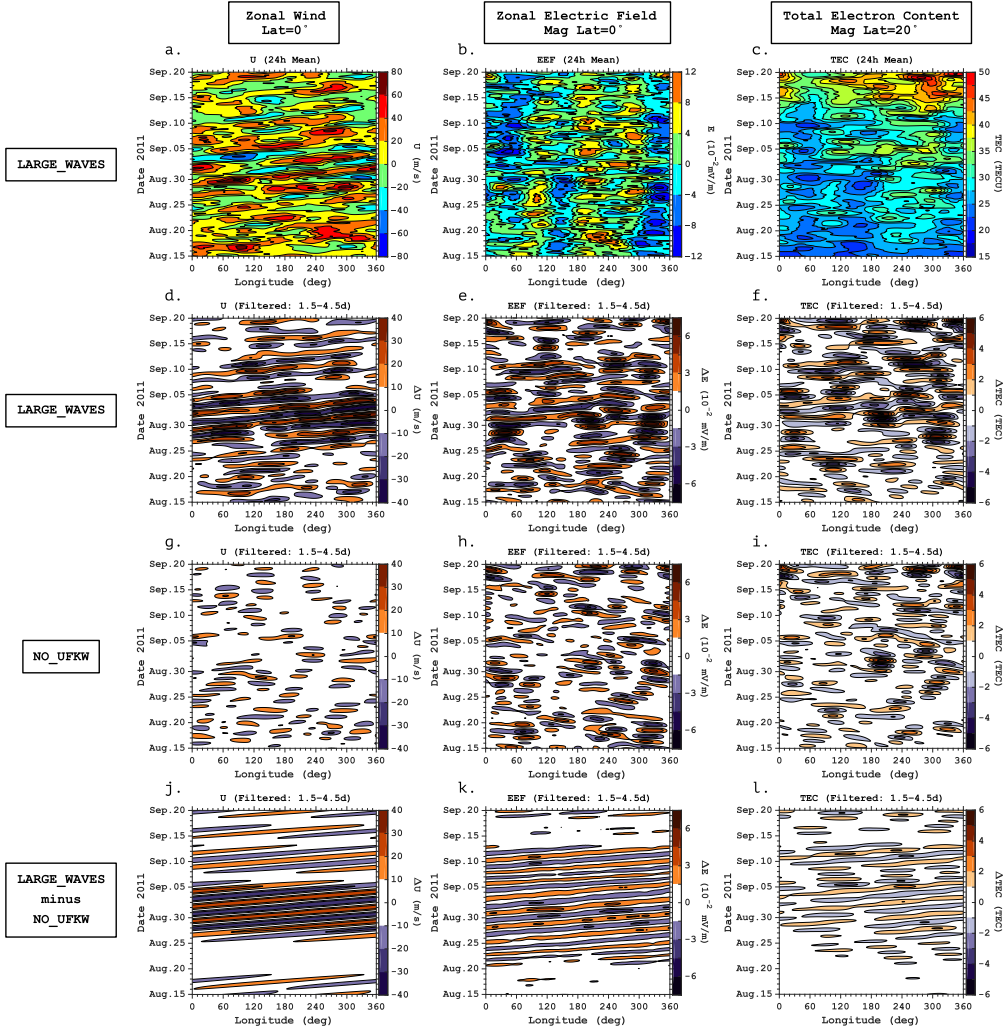


Figure 13. (a–c) Longitude versus time diagrams for the 24h mean of (a) the equatorial zonal wind at 110 km altitude, (b) equatorial zonal electric field (EEF) at 110 km altitude, and (c) total electron content (TEC) derived from the LARGE_WAVES simulation case. (d–e) The same as (a–c) but the 1.5–4.5d bandpass filter is applied at each longitude to extract \sim 3-day variations. (g–i) The same as (d–e) except for the NO_UFKW simulation case. (j–l) The difference between LARGE_WAVES and NO_UFKW simulation cases, isolating the effect of the ultra-fast Kelvin wave.

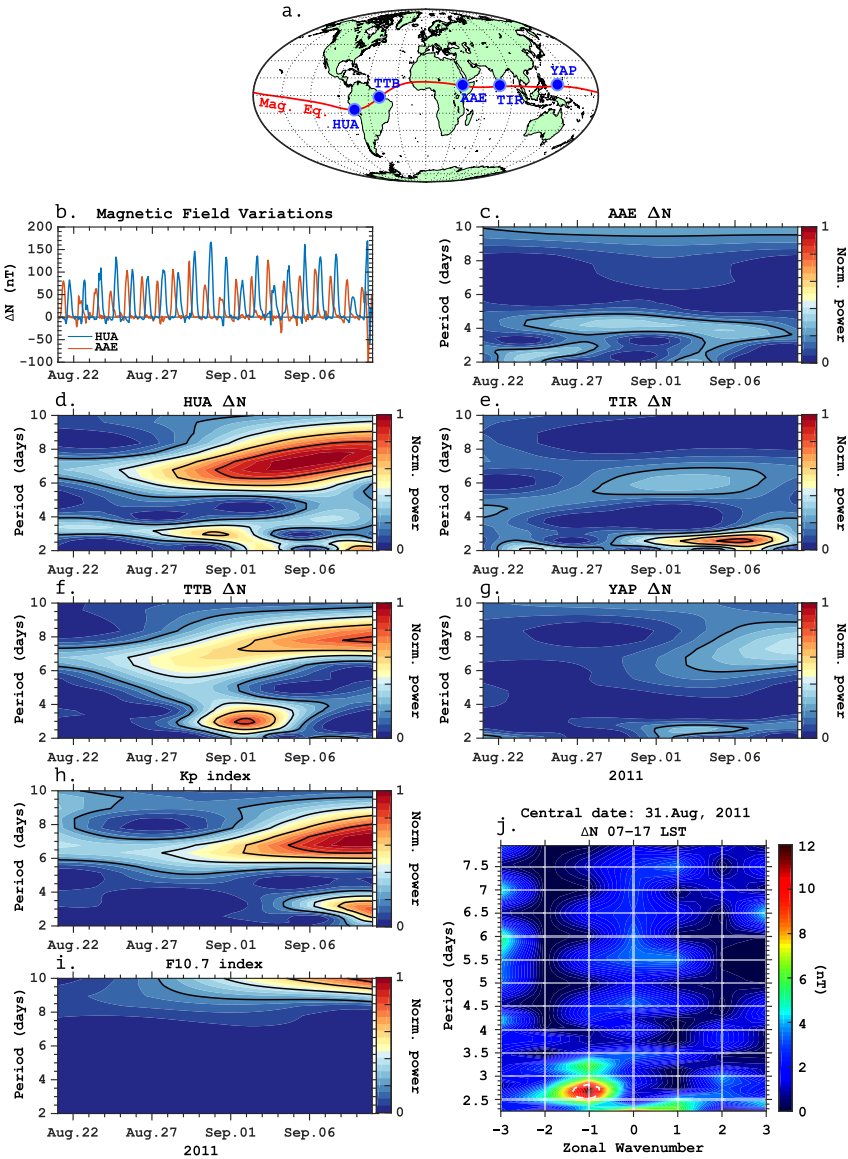


Figure 14. (a) Locations of the magnetic observatories: HUA=Huancayo; TTB=Tatuoca; AAE=Addis Ababa; TIR=Tirunelveli; and YAP=Yap Island. The red line denotes the magnetic equator. (b) Examples of magnetic field perturbations in the magnetic-northward component (ΔN) at Huancayo and Addis Ababa during 21 August–9 September. (c–g) Wavelet spectra of ΔN at different observatories as a function of time and period. Spectral power is normalized to the maximum value at Huancayo. (h) Wavelet spectrum of the geomagnetic activity index K_p . Spectral power is normalized to the maximum value. (i) Wavelet spectrum of the solar activity index $F_{10.7}$. Spectral power is normalized to the maximum value. (j) Wavenumber versus period spectrum of ΔN derived from the combination of the daytime ΔN data from the five observatories. The white dashed lines correspond to the 95% confidence level.

Table 1. The numerical experiments performed in this study and the wave forcing used therein.

Experiment	Waves
LARGE_WAVES	E5–W5, all periods
NO_UFKW	Same as LARGE_WAVES but excludes E1 with period 1.5–4.5d

Table 2. Zonal wavenumber s and period τ (days) of the global-scale waves from which aliasing into the ultra-fast Kelvin wave ($s=-1$, $\tau=2\text{--}4$ days) spectral component can occur when the wave signatures are sampled at a fixed local solar time. Aliasing effects are reduced when the wave signatures are sampled over a range of local solar time (e.g., 3h, 6h, 12h), which is expressed in terms of the amplitude ratio γ with respect to the amplitude calculated by sampling wave signatures at a single local time. Possible sources of aliasing are also indicated, where the X mark represents the non-linear interaction between the ultra-fast Kelvin wave (UFWK) and migrating tides, with S1, S2, S3, S4, and S5 signifying $n=1$ (diurnal tide), $n=2$ (semidiurnal tide), $n=3$ (terdiurnal tide), $n=4$, and $n=5$, respectively, and the Q2DW standing for the quasi-2-day wave.

s	τ	γ_{3h}	γ_{6h}	γ_{12h}	Possible sources
0	0.67–0.80	0.97	0.90	0.64	UFWK × S1
+1	0.40–0.44	0.90	0.64	0.00	UFWK × S2
+2	1.33–2.00	0.97	0.90	0.64	Q2DW, UFWK × S1
+2	0.29–0.31	0.78	0.30	0.21	UFWK × S3
+3	0.57–0.67	0.90	0.64	0.00	UFWK × S2
+3	0.22–0.24	0.64	0.00	0.00	UFWK × S4
+4	0.36–0.40	0.78	0.30	0.21	UFWK × S3
+4	0.18–0.19	0.47	0.18	0.13	UFWK × S5